ELSEVIER

Contents lists available at ScienceDirect

Composite Structures

journal homepage: www.elsevier.com/locate/compstruct





Multiscale damage modelling of notched and un-notched 3D woven composites with randomly distributed manufacturing defects

S.Z.H. Shah a , Juhyeong Lee b , P.S.M. Megat-Yusoff a , Syed Zahid Hussain c , T. Sharif d , R. S Choudhry d,*

- ^a Department of Mechanical Engineering, Universiti Teknologi PETRONAS, 32610 Bandar Seri Iskandar, Perak, Malaysia
- b Department of Mechanical and Aerospace Engineering, Utah State University, Logan, UT 84322-4130, USA
- ^c Department of Mechatronics Engineering, Air University, E-9 Islamabad, Pakistan
- d School of Computing and Engineering, Mechanical Engineering Discipline, University of Derby, UK

ARTICLE INFO

Keywords: Multiscale Stochastic Progressive damage model 3D woven fabric composites Thermoplastic

ABSTRACT

This work proposes a stochastic multiscale computational framework for damage modelling in 3D woven composite laminates, by considering the random distribution of manufacturing-induced imperfections. The proposed method is demonstrated to be accurate, while being simple to implement and requiring modest computational resources. In this approach, a limited number of cross-sectional views obtained from microcomputed tomography (µCT) are used to obtain the stochastic distribution of two key manufacturing-induced defects, namely waviness and voids. This distribution is fed into a multiscale progressive damage model to predict the damage response of three-dimensional (3D) orthogonal woven composites. The accuracy of the proposed model was demonstrated by performing a series of finite element simulations of the un-notched and notched tensile tests (having two different hole sizes) for resin-infused thermoplastic (Elium®) 3D woven composites. Excellent correlation was achieved between experiments and the stochastic finite element simulations. This demonstrates the effectiveness of the proposed stochastic multiscale model. The model successfully captured the stochastic nature of tensile responses (ultimate tensile strength and stiffness), damage modes (matrix damage and fibre failure), and initiation and propagation of transverse cracks in thermoplastic 3D woven composites, consistent with experimental observation. The stochastic computational framework presented in this paper can be used to guide the design and optimization of 3D textile composite structures.

1. Introduction

Accurate and fast predictive modelling of damage tolerance in fibre-reinforced composite materials has been an active topic of interest for researchers and industry for many decades [1,2]. A progressive damage model, which is realistic, easy to implement and computationally highly efficient, on one hand, can be used as a generative design tool for new product development and on the other, for creating digital twins for structural health monitoring and predictive maintenance. While significant success has been achieved for damage modelling of unidirectionally (UD) reinforced laminates as well as multidirectional stacks of UD lamina using conventional (single scale) continuum damage mechanics models [3,4]; major challenges still impede such development for composites with more complicated reinforcement architecture such as the 3D fabric composites. For example, due to the complexity of the

architecture and the significantly different nature of progressive damage, the progressive damage in each constituent must be simulated independently. To address this challenge researchers have often resorted to micromechanics-based models. In a pure micro-mechanics approach either an idealized or near to realistic [5], periodically repeating representative volume element (RVE) is considered and the elastic response, as well as strengths of the homogenized medium, are predicted based on this RVE model [6–8]. This approach is contentious because the damage growth process does not repeat periodically across the structure and therefore the damage growth response based on periodic homogenisation strategies is unrealistic. If a full-scale FE model of the entire structure is built using such approaches then that becomes computationally very demanding even for moderately sized parts due to the need for a very high mesh density. For example, the work done by Green et al. [5] reported a five-day running time of the model for a

E-mail address: r.choudhry@derby.ac.uk (R.S Choudhry).

^{*} Corresponding author.

 $27.8 \times 9.9 \times 5.3$ mm³ RVE just with the baseline mesh. One could easily imagine the months of simulation time required for even a moderately sized part. To address these limitations a series of multiscale methods have been developed. One possible approach for multiscale modelling involves two finite element (FE) simulations - one at the microscale and the other at the macroscale for uni-directional composites [9] or at the meso-scale for multidirectional (textile) composites [9] – carried out in a nested manner, also called the FE² method. This method is computationally very expensive, particularly for large-scale dynamic simulations [10,11]. To improve the efficiency of FE² methods, some new approaches have been proposed recently, such as the work of Spahn et al. [12] and Huang et al. [13]. Other alternate multiscale modelling methodologies have also been presented and a summarised review of the various strategies for multiscale modelling of composites is presented in our earlier publication [14]. In that work, a new deterministic multiscale modelling framework for 3D composites was presented. In that approach [14] the global or part-level FE analysis is performed at the macro-scale, while the damage initiation was predicted at the meso-scale using an analytical meso-scale unit-cell/RVE model of a 3D woven composite. The damage evolution, in that case, was modelled separately in impregnated varns and matrix regions. This approach provided a high level of computational efficiency at a reasonable level of accuracy. For example, a typical runtime for a tensile test simulation in [14] for a specimen size of 8000 elements is around 30 min (4 CPU cores). This approach can be easily extended to any part size. Although the approach efficiently solves the challenges of the heterogeneity and non-periodicity of damage progression, it is still limited in accuracy because the initial input elastic and geometric properties of RVE are assumed to be the same for every region of the global part model. This assumption is not completely true because even when one uses advance NDT techniques, like X-ray CT to accurately model the geometric microstructure for an RVE there will be local variations in effective mechanical properties from one unit-cell (RVE) to the other due manufacturing limitations and changing contours of part geometry. In practice, the geometrical imperfection or defects, such as matrix voids, resin-rich pockets, fibre spatial distribution, fibre misalignment, local variability in the fibre volume fraction, waviness in yarn's cross-section, which mainly arise as a consequence of the manufacturing processes [15-20], cause local variations of effective mechanical properties of unit-cell (RVE). A better and more accurate modelling framework must take into account these manufacturing-induced variabilities, which are typically observed in real composites, while still keeping the computational cost low. Thus in this paper, our focus is presenting the development and validation of such a novel multiscale model that indirectly accounts for local and global variations in geometric and material property uncertainties without making the model significantly computationally demanding.

In textile composites, the macro-scale variabilities in effective mechanical properties such as stiffness and strength are manifestations of commutative defects that exist at a sub-scale level, i.e., micro- and mesoscales [21–23]. The quantification of variabilities at the sub-scale level and subsequent propagation to the macro-scale (or component level) is crucial for the stochastic multiscale analysis of textile composite. With the advancement of micromechanics-based homogenization theories, researchers have now a better understanding of the relationships between sub-scale and macro-scale composites [24]. Zhang et al. [25] proposed a multiscale progressive damage model based on a local-–global (mesoscale-macroscale) method to predict the flexural response of 3D hybrid composites. However, authors did not account manufacturing induced defects in the local (mesoscale) model. In recent years, it has enabled researchers to establish several stochastic predictive models, to predict variabilities in mechanical properties by incorporating uncertainties at different length scales [10,19,26,27]. In this regard, a detailed review of the stochastic multiscale analysis of composites is given by Zhou et al. [21]. The authors concluded that the existing multiscale models did not consider manufacturing defects and their resulting variabilities were not successfully implemented in a

realistic way.

Several authors proposed stochastic multiscale approaches to predict the mechanical properties of two-dimensional (2D) textile composites [27-34]. In these models, uncertainties in material properties were introduced in a micro-scale unit-cell model and the FE simulations were performed at meso-scale, which makes these approaches computationally expensive for large-scale or component-level simulation. Patel et al. [32,33] developed a multiscale progressive damage model to predict the tensile and compressive responses of hybrid 3D textile composites. The authors generated a mesoscale FE model using μ CT data; thus, the model considers manufacturing-induced defects. However, the mesoscale model is directly generated from µCT data, which is computationally inefficient and not practical for component-level analysis. Recently, Wei et al. [16] proposed a stochastic multiscale model considering local variabilities of material properties at the micro- and meso-scales to predict the macroscopic response of 3D composites. In the proposed approach, the macro-scale analysis was performed using the shell model, which is not suitable to predict the through-thickness damage response of 3D textile composites. Han et al. [17] developed a multiscale model using the probabilistic distribution of fibre modulus and voids to predict the stochastic response of 3D braided textile composites. The authors did not consider waviness in individual impregnated varns caused during manufacturing processes. Similarly, Lei et al. [18] and Huang et al. [35] proposed a stochastic multiscale model for 3D textile composites by considering voids defects only. In recent years, researchers have also proposed coupled data-driven multiscale uncertainty quantification and propagation frameworks, to predict the mechanical performance of textile composites [16,36–38]. Additionally, several authors proposed a computational framework based on coupled unit-cell/RVE homogenization and the Monte-Carlo method to predict the effect of uncertainties on the effective properties of fibre-reinforced composites (FRCs) [26,39-41].

This review of literature highlighted that for 3D composites, there is a need to develop a strategy for component-level multiscale damage simulations that can account for manufacturing-induced variability in part quality and while doing so is also computationally less demanding and easy to set up. Thus in this paper we aim to address this dual challenge and propose a strategy that involves (a) realistic statistical quantification of manufacturing induced random geometrical variabilities (i.e., localized geometrical imperfection or defects) at the sub-scale level, (b) propagating this statistical information in the virtual sub-scale model (i.e., at the two-scales (micro-scale and meso-scale)) and generate stochastic material properties for the macro model), (c) perform stochastic multiscale progressive damage analysis to predict damage response of textile composites and d) carry out a global part level finite element simulation of the test case in a reasonable time frame. In this paper, we demonstrate the use of this strategy for both un-notched and notched 3D composites with excellent correlation with experimental

This paper is organised as follows. In Section 2, we explain the details of the stochastic multiscale progressive damage model for textile composites. In Section 3, we discuss the experimental evaluations of the unnotched and notched response of 3D woven composites. In Section 4, we explain the FE implementation of the framework and show how it is applied to simulate the damage response of un-notched and notched composites. In Section 5, we establish the predictive capabilities of the proposed modelling framework by comparing it with the experiments described in Section 2. Finally, we summarise the conclusions in Section 6.

2. Stochastic multiscale progressive damage model

Fig. 1 shows the overall flowchart of the proposed stochastic multiscale progressive damage model. The model consists of four main steps, i.e., (a) a *stochastic material model* to generate a normal distribution of waviness in impregnated yarns and voids in a polymer matrix; (b) a

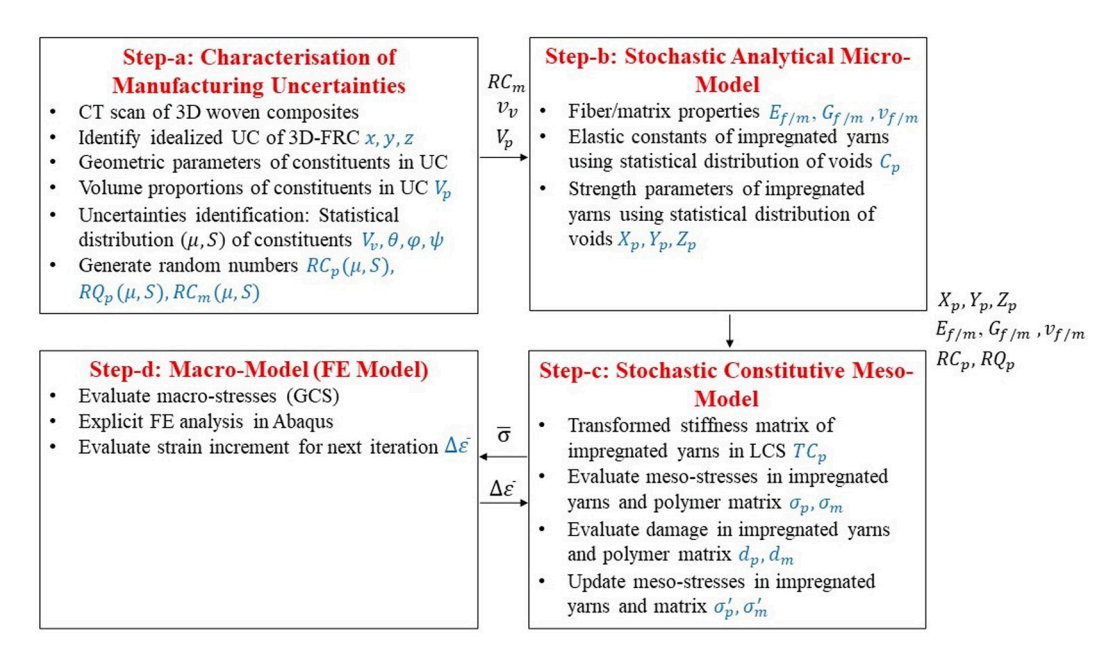


Fig. 1. Stochastic multiscale progressive damage model. x, y, z = Dimension of unit-cell (UC); p = Impregnated warp, weft, and binder yarns; $V_p = \text{Volume proportions of the constituent}$; $\theta, \varphi, \psi = \text{Waviness in impregnated yarns (see Table 1 and Fig. 2)}$; $V_p = \text{Void content}$; $RC_p, RC_m, RQ_p = \text{Random numbers }(R)$ for stiffness (C) & strength (Q); $\Delta \bar{e} = \text{Macro-strains in GCS}$; $\bar{\sigma} = \text{Macro-stresses in GCS}$; $\Delta e^p = \text{Meso-strains in LCS}$.

stochastic analytical micromechanics model to generate a corresponding normal distribution of elastic constants and strength properties of impregnated yarns, using fibre volume fraction, elastic constants and strength properties of fibre and polymer matrix. These normal distributions are fed into the meso-model to evaluate the damage state of each constituent; (c) a stochastic constitutive meso-model of 3D woven composites to evaluate for each unit-cell a unique stiffness matrix corresponding to the unique set of parameters (elastic constants and waviness) obtained in steps a and b; and (d) a macro-scale explicit dynamic FE model of 3D woven composites to determine homogenized macro-stresses on the component being virtually tested in a global coordinate system (GCS). The models in steps c and d have a bidirectional flow of information. Thus, the macro-model (step d) is used to provide the strain increment for each material integration point within the FE mesh to the unit-cell model (step c). The macro model is then updated by evaluating the meso-stresses and damaged state of each constituent in a local coordinate system (LCS) using the unique stiffness matrix for that unit cell. The process is repeated for each unit cell within the macro model for each time increment.

All the sub-models (steps a–c) used to describe the stochastic variation in material properties are coupled to the macro-model (step d) for finite element implementation through a user-defined material subroutine. In this study, we have achieved this using a vectorized user material (VUMAT) subroutine in Abaqus/explicit. The approach, however, is generic and may be implemented in other FE software that allows for user-defined material behaviour. Details of each of these sub-models are presented in the following sections.

2.1. Characterisation of manufacturing uncertainties for material model

The development of a stochastic material model required accurate identification of geometric uncertainties present in fabricated composites. Therefore, μ CT was undertaken to quantify inherent geometric uncertainties produced by the composite manufacturing process. Using μ CT it is possible to generate detailed 3D model of a localised region within the composite and several researchers have used this to directly create the 3D micro and *meso*-level unit cell [42–44]. This approach is not pursued in this study because the unit cell generated from a single scanned region is not necessarily representative of the variations in the

entire sample. In order to obtain a better representation of the random distribution of defects within the entire specimen, we have used multiple cross-sectional views from randomly selected sampling points from various locations in a representative test piece. Thus, Fig. 2 shows a typical cross-sectional µCT images of 3D orthogonal woven composites used in this study. The resolution and filter used during to are $28\,\mu m$ and LE2 (Low Energy filter 2), respectively. These images were used to manually determine the mean (μ) and standard deviation (S) of waviness in impregnated warp varn (θ) , weft varn (φ) and binder varn (ψ) , respectively, as summarised in Table 1. The S of yarn waviness is obtained from seven different cross-sections along the warp and fill direction. The waviness along the warp and weft directions is measured using the same method. The void content of fabricated 3D orthogonal woven composites is measured using the burn-off method [45]. The variabilities in the void content among ten different samples are also given in Table 1.

The stochastic material model was implemented within the VUMAT subroutine and was called at every time increment for each unit cell in the macro-FE model to generate a uniform, random distribution of waviness in impregnated yarns and voids in the matrix and to evaluate the corresponding stochastic distribution in the elastic constants and strength properties. Fig. 3 depicts the proposed algorithm's pseudocode, which generates a stochastic distribution of elastic constants and strength properties for the *meso*-scale model. The code requires inputs of the number of unit-cells (n) in the macro-model, and the mean (μ) and standard deviation (S) of the waviness of warp, weft, and fill yarns, and void content (see Table 1). The Box-Muller (BM) transformation algorithm [46] is then employed to obtain the Gaussian distribution of random material properties. The BM algorithm generates an independent random variable (Z) with a standard normal distribution, given by Eq. (1).

$$Z(0,1) = \sin(2\pi R_1) \sqrt{-2\ln(R_2)} \tag{1}$$

where, R_1 and R_2 are uniformly distributed random numbers on a unit interval [0, 1]. The uniformly distributed random variable (Z) is then scaled based on the mean (μ) and standard deviation (S) of properties (elastic constants and strength properties) in a specific range, i.e.,

$$RQ_{ij,p}^{n}(\mu, S) \text{ or } RC_{ij,p}^{n}(\mu, S) = \mu_{ij} \pm S_{ij} \times Z_{1}(0, 1)$$
 (2)

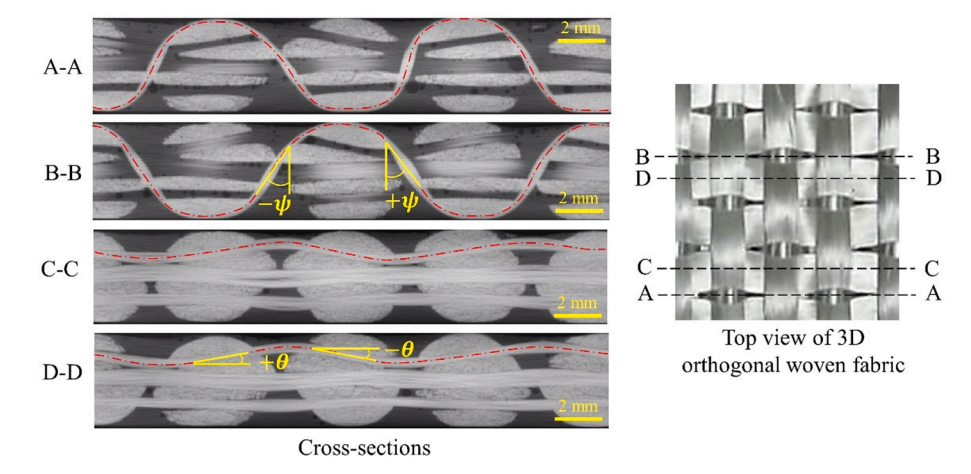


Fig. 2. Cross-sectional μ CT images of 3D-FRC with waviness along the warp yarn (θ) and the binder yarn (ψ).

Table 1
Mean and standard deviation of waviness in impregnated yarn and voids.

			•
Scale	Uncertainty sources	Mean value (μ)	Standard deviation (σ)
Meso- scale	Waviness in the warp yarn " θ "	O°	7.3°
	Waviness in the fill yarn " ϕ "	90°	7.5°
	Waviness in the binder yarn " ψ "	90°	30.5°
Micro- scale	Voids " V_{ν} "	2.7 %	1.1%

where Q^n_{ijp} and C^n_{ijp} each represents a value of randomly generated strength properties and elastic constants (Youngs's moduli, shear moduli and Poisson's ratios) in the three principal directions. The python code assigns these properties (Q^n_{ijp} and C^n_{ijp}) to the n^{th} unit cell in the model, which in this study corresponds to the n^{th} finite element in the mesh. This process is repeated until random properties were assigned to all the unit cells defining the part (i.e., the entire finite element mesh), consistent with our previous work [47]. It should be pointed out that in this study the choice of Gaussian distribution to represent yarn waviness was based on a previous study [48]. The close correlation with the results in later sections, however, further demonstrates that this was a reasonable assumption. Had this proved insufficient to capture the strength distribution at the global level then the model could have been improved by first identifying the appropriate distribution from a statistical test like Kolmogorov-Smirnov or Shapiro-Wilk.

2.2. Stochastic analytical micro-model

The impregnated warp, fill, and binder yarns were treated as transversely isotropic materials, which means that their elastic response could be described by five elastic constants. The elastic constants and their corresponding strength properties can be evaluated either using a FE micro-mechanics model or an analytical micro-mechanical model. In the proposed stochastic multiscale model a unique set of elastic constants and strength properties of impregnated yarns were determined for each unit-cell corresponding to the stochastic distribution of void volume fraction V_{ν} in the unit cell. This was done by using uniformly distributed random numbers generated by the stochastic material model (Section 2.1) to represent the changing values of void volume fraction

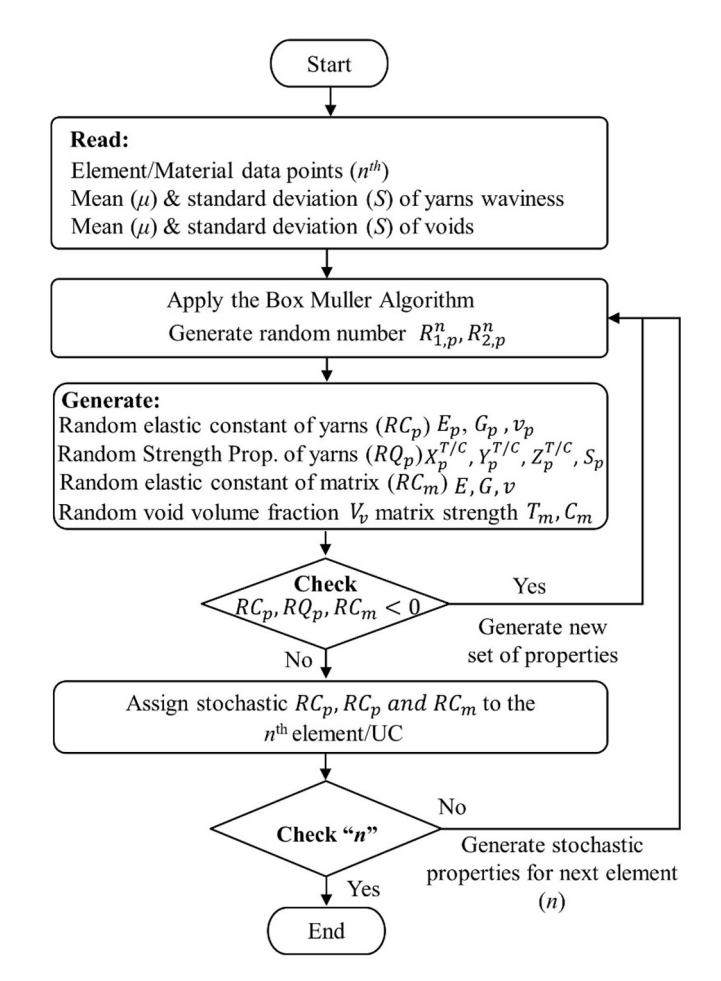


Fig. 3. Sudo-code algorithm for stochastic material property generation and assignment.

 (V_{ν}) in the Chamis model (Eq. (3)) [49]. In doing so, it was assumed that the elastic constants and strength properties of the polymer matrix were degraded linearly with void volume fraction. These properties were then used by the *meso*-model to evaluate a unique stiffness matrix, *meso*-stress and the damaged state of each impregnated yarn.

$$\begin{cases} E_{11,p}^{n} = V_{f,p}E_{11f} + V_{m}E_{m}(1 - V_{v}^{n}) \\ E_{22,p}^{n} = E_{33,p}^{n} = \frac{E_{m}}{1 - \sqrt{V_{f,p}}} \left(1 - \frac{E_{m}(1 - V_{v}^{n})}{E_{22f}}\right) \\ G_{12,p}^{n} = G_{13,p}^{n} = \frac{G_{m}(1 - V_{v}^{n})}{1 - \sqrt{V_{f,p}}} \left(1 - \frac{G_{m}(1 - V_{v}^{n})}{G_{12f}}\right) \end{cases}$$

$$G_{23,p}^{n} = \frac{G_{m}(1 - V_{v}^{n})}{1 - \sqrt{V_{f,p}}} \left(1 - \frac{G_{m}(1 - V_{v}^{n})}{G_{23f}}\right)$$

$$v_{12,p}^{n} = V_{f,p}v_{f} + V_{m}v_{m}(1 - V_{v}^{n})$$

$$v_{23,p}^{n} = \frac{E_{22,p}^{n}}{2G_{23,p}^{n}} - 1$$

where $V_{f,p}$, V_m , and V_v^n each denotes the fibre volume fraction of impregnated yarns, matrix volume fraction, voids volume fraction of n^{th} element; v_f , E_f , and G_f indicates Poisson's ratio, elastic modulus, and shear modulus of the fibres, while v_m , E_m , and G_m are those for the matrix; E_{11p}^n , E_{22p}^n , E_{33p}^n , G_{12p}^n , G_{33p}^n , V_{12p}^n , and V_{23p}^n represent the effective (bulk) elastic and shear moduli, and Poisson's ratio of the impregnated yarns for n^{th} element in a local coordinate system (LCS). Similarly, the strength properties of impregnated yarns are estimated using the Chamis model [49] given by Eq. (4).

$$\begin{cases} X_{11,p}^{T,n} = V_{f,p}X_{f}^{T} \\ X_{11,p}^{C,n} = V_{f,p}X_{f}^{C} \end{cases} \\ X_{22,p}^{C,n} = \left[1 - \left(\sqrt{V_{f,p}} - V_{f,p}\right) - \frac{E_{m}(1 - V_{v}^{n})}{E_{22,f}}\right] T_{m} \left(1 - V_{v}^{n}\right) \\ X_{22,p}^{C,n} = \left[1 - \left(\sqrt{V_{f,p}} - V_{f,p}\right) - \frac{E_{m}(1 - V_{v}^{n})}{E_{22,f}}\right] C_{m} \left(1 - V_{v}^{n}\right) \\ S_{12,p}^{n} = \left[1 - \left(\sqrt{V_{f,p}} - V_{f,p}\right) - \left(1 - \frac{G_{m}(1 - V_{v}^{n})}{G_{12,f}}\right)\right] S_{m} \left(1 - V_{v}^{n}\right) \\ a \end{cases}$$

where $X_{11p}^{T,n}$, $X_{11p}^{C,n}$, $X_{22p}^{T,n}$, $X_{22p}^{C,n}$ and S_{12p}^{n} represents longitudinal tensile strength, longitudinal compressive strength, transverse tensile strength, transverse compressive strength, and in-plane shear strength, respectively, of the impregnated yarns for n^{th} element in LCS. X_f^T and X_f^C each denotes the tensile and compressive strength of the fibre. T_m , C_m and S_m refers to the tensile, compressive and shear strength of the matrix, respectively.

2.3. Stochastic constitutive meso-model (unit-cell model)

The stochastic constitutive *meso*-model is the most important part of the stochastic, multiscale, progressive damage modelling framework. It takes the normal distributions of impregnated yarn and polymer matrix properties from the micro-model and the normal distribution of waviness in each impregnated yarn from the stochastic material model as an input. These inputs are utilized in evaluating the unique stiffness matrix and *meso*-stresses of each constituent of the *meso*-model using appropriate transformation equations. The *meso*-stresses are then used to determine the damage response of impregnated yarns and the polymer matrix using appropriate failure criteria. The proposed stochastic *meso*-model was developed to address the limitations of our previous deterministic *meso*-model [14] of 3D woven composite (Fig. 4), i.e., (a) impregnated yarns are not necessarily perfectly perpendicular to each

other, (b) each impregnated yarn contains waviness and (c) there are voids in the resin-rich pockets. Therefore, the proposed stochastic *meso*-model is a non-idealised unit-cell model and represents the actual internal architecture of a 3D woven composite.

To mimic the physical reality, each element in the macro-FE model is associated with a stochastically unique meso-model (or unit-cell) in the multiscale model. The uniqueness of the meso-model is a consequence of the differences in the varn waviness and voids in resin-rich pockets for each unit cell. Thus, each impregnated yarn in the meso-model is assigned with unique elastic constants and strength properties from the stochastic analytical micro-model (Eqs. (3) and (4)), which results in unique effective elastic and strength constants for each instance of the unit-cell model. This means that, unlike a traditional FE mesh where only one set of material properties is assigned initially to the macromodel mesh, the elastic response and damage state of each element in the macro-model for the stochastic multi-scale model are different. Similarly, the damage also develops independently in each unit-cell and the constitutive meso-model is called by the macro-model explicit FE solver at each integration point to update the damage index of the 3D-FRC part being virtually simulated.

2.3.1. Damage modelling of impregnated yarn

The 3D orthogonal woven composites ideally consist of three perpendicular impregnated yarns (warp, weft and binder). In this work, each yarn was locally treated as a transversely isotropic material and analytically modelled according to their orientation and volume fraction in a unit cell (Fig. 4). The constitutive model of impregnated yarns was transformed from local (123) to a global (XYZ) coordinate system, using Eq. (5).

$$\sigma_{ij}^{G} = \left[T_{p}^{n,G|L}\right]^{T} \sigma_{ij}^{L}$$

$$\varepsilon_{ij}^{G} = \left[T_{p}^{n,G|L}\right]^{T} \varepsilon_{ij}^{L}$$

$$C_{ij}^{n,G} = \left[T_{p}^{n,G|L}\right]^{-1} \left[C_{ij}^{n,L}\right] \left[T_{p}^{n,G|L}\right]^{-T}$$

$$(5)$$

where ij are 1, 2, and 3, and p= warp, weft, and binder yarns. σ^L_{ij} , ε^L_{ij} , and $G^{n,L}_{ij}$ represents the stress vector, strain vector, and stiffness tensor in the local coordinate system (123), respectively. σ^G_{ij} , ε^G_{ij} , and $G^{n,G}_{ij}$ each denotes the stress vector, strain vector, and stiffness tensor in the global coordinate system (XYZ). $T^{n,G|L}_p$ depicts the unique transformation matrix for each impregnated yarn from the local to the global coordinate system, defined as yarn orientations, i.e., θ^n , φ^n , and φ^n . The transformation matrix for the warp and weft yarn is given by Eq. (6).

$$\left[T_p^{n,G|L}\right] = \begin{bmatrix} \cos^2 \omega^n & \sin^2 \omega^n & 0 & 0 & 0 & 2\cos\omega^n \sin\omega^n \\ \sin^2 \omega^n & \cos^2 \omega^n & 0 & 0 & 0 & -2\cos\omega^n \sin\omega^n \\ 0 & 0 & 1 & 0 & 0 & 0 \\ 0 & 0 & 0 & \cos\omega^n & -\sin\omega^n & 0 \\ 0 & 0 & 0 & \sin\omega^n & \cos\omega^n & 0 \\ -\cos\omega^n \sin\omega^n & \cos\omega^n \sin\omega^n & 0 & 0 & 0 & \cos^2 \omega^n - \sin^2 \omega^n \end{bmatrix}$$

where omega ω^n is the angle of warp and weft yarns, between global and local coordinate systems, which is ideally $\omega^n = \theta^n = 0^\circ$ and $\omega^n = \varphi^n = 90^\circ$ counter-clockwise, respectively. The transformation matrix for binder yarn is given by Eq. (7).

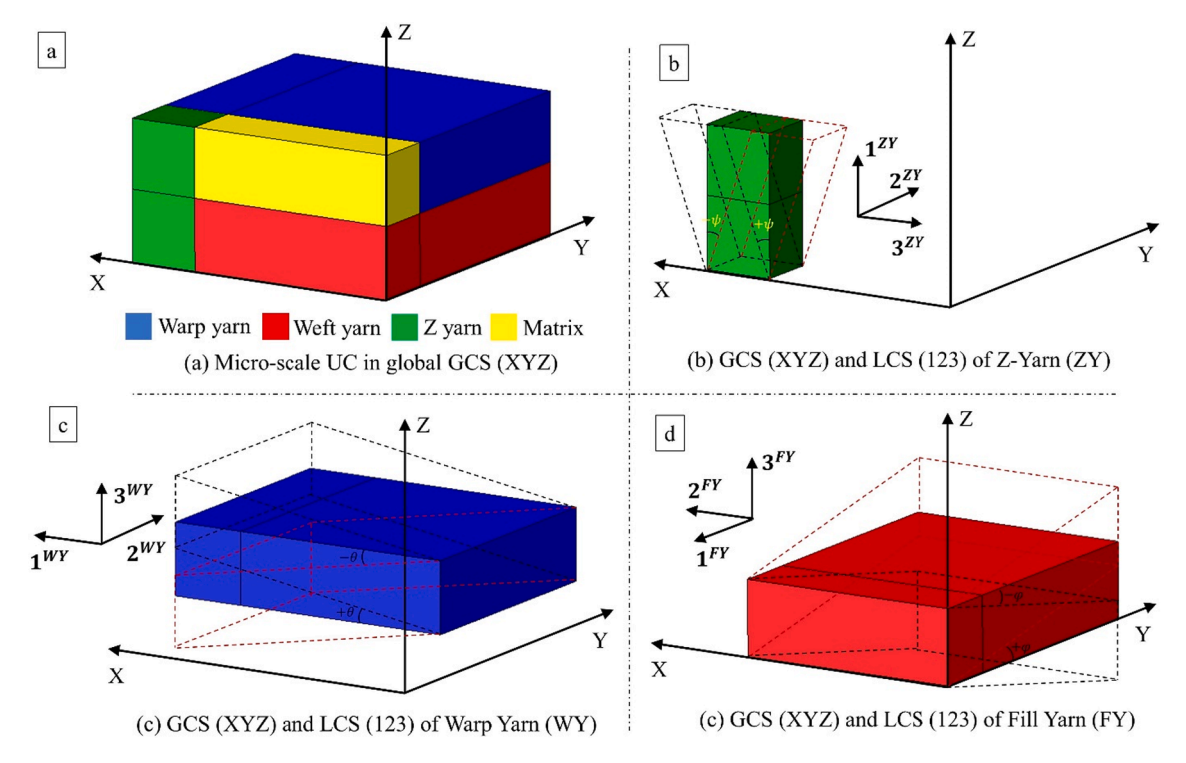


Fig. 4. Idealized 3D woven composite unit-cell model. The dotted lines in the figures represent yarn waviness.

$$\left[T_p^{n,G|L}\right] = \begin{bmatrix} \cos^2\psi^n & 0 & \sin^2\psi^n & 0 & 2\cos\psi^n\sin\psi^n & 0\\ 0 & 1 & 0 & 0 & 0 & 0\\ \sin^2\psi^n & 0 & \cos^2\psi^n & 0 & -2\cos\psi^n\sin\psi^n & 0\\ 0 & 0 & 0 & \cos\psi^n & 0 & -\sin\psi^n\\ -\cos\psi^n\sin\psi^n & 0 & \cos\psi^n\sin\psi^n & 0 & \cos^2\psi^n - \sin^2\psi^n & 0\\ 0 & 0 & 0 & \sin\psi^n & 0 & \cos\psi^n \end{bmatrix}$$

where, angle ψ^n is the angle binder yarn angle, between global and local coordinate systems, which is ideally $\psi^n = -90^\circ$ (clockwise). There are two main differences between our previous damage model in [14] and the current work: (1) θ^n , ϕ^n , and ψ^n are no longer constant parameters and instead vary in accordance with the values computed from Eqs. (2) and (2)) the impregnated yarn failure initiation strengths also exhibit stochastic variations as explained earlier (Eqs. (3) and (4)). This ensures that the stochastic variation of these parameters as observed in real composites is captured and thus the model is more realistic as compared to our earlier model [14].

The damage response of impregnated yarns was modelled as linear elastic until damage initiation, followed by linear damage evolution. Modified 3D quadratic failure criteria [14] were employed to predict damage initiation in each impregnated yarn. On the onset of damage, the stiffness of damaged yarns was degraded according to the linear damage evolution law (see Fig. 5a), given by Eq. (8), which is used to update the damage stiffness matrix of impregnated yarns.

$$d_{i,T} = \left(\frac{\varepsilon_{i,T}^f}{\varepsilon_{i,T}^f - \varepsilon_{i,T}^{ini}}\right) \left(\frac{\varepsilon_{i,T} - \varepsilon_{i,T}^{ini}}{\varepsilon_{i,T}}\right) \tag{8}$$

$$d_{i,C} = \left(rac{arepsilon_{i,C}^f}{arepsilon_{i,C}^f - arepsilon_{i,C}^{imi}}
ight) \left(rac{arepsilon_{i,C-}arepsilon_{i,C}^{imi}}{arepsilon_{i,C}}
ight)$$

where, $\varepsilon_{i,T}^{ini}$, $\varepsilon_{i,T}^{i}$, and $\varepsilon_{i,T}^{f}$ represent the strain value at damage initiation, current strain and strain at the final damage state under tensile (*T*) load, respectively. $\varepsilon_{i,C}^{ini}$, $\varepsilon_{i,C}^{i}$, and $\varepsilon_{i,C}^{f}$ represent the strain value at damage

initiation, current strain and strain at the final damage state under compressive (C) load, respectively. The subscript i=1, 2, and 3 represents the longitudinal, in-plane transverse, and out-of-plane transverse directions. The micro-stresses σ_{ij}^f in individual yarns were updated using the damaged stiffness matrix $C_{ij}^{D,f}$ and micro-strains ε_{ij}^f , given by Eqn. (9).

$$\sigma_{ij}^f = C_{ij}^{Df} \varepsilon_{ij} \tag{9}$$

2.3.2. Damage modelling of polymer matrix

The polymer matrix was considered an isotropic material. The tensile and compressive yield strengths of the polymer matrix may be different due to the dependency of yielding on the hydrostatic components of the applied stress state. Therefore, a modified von Mises failure criteria in terms of tensile and compressive strength is given by Eq. (10).

$$\frac{\sigma_{v}^{2}}{C_{m}T_{m}} + \left(\frac{1}{T_{m}} - \frac{1}{C_{m}}\right)I_{1} = 1 \tag{10}$$

where C_m , T_m , σ_v , and I_1 represent the compressive and tensile strengths of the polymer matrix, von Mises stress and the first stress invariant, respectively. Prior to damage initiation, the response of pure matrix is treated as linear elastic, followed by elastoplastic deformation occurring as a result of damage growth (Fig. 5b). The matrix damage evolution used in this work is based on the multi-linear damage evolution law proposed by Xu et al. [50], where yield stress and equivalent strain relationship are used to evaluate the damage state for each step, given by Eq. (11).

$$d_{m}^{q} = \frac{\sigma_{y}^{q-1} \left(\varepsilon_{y}^{q} - \varepsilon_{eq}\right) + \sigma_{y}^{q} \left(\varepsilon_{eq} - \varepsilon_{y}^{q-1}\right)}{E_{0,m} \varepsilon_{eq} \left(\varepsilon_{y}^{q} - \varepsilon_{y}^{q-1}\right) (1 - V_{y})}$$

$$(11)$$

where ε_y^q , ε_y^{q-1} , σ_y^q , σ_y^{q-1} and ε_{eq} represent yield strain at the damage stage q, yield strain at the damage stage q-1, yield stress at the damage stage q-1, and equivalent strain in ith damage stage ($\varepsilon_y^{q-1} < \varepsilon_{eq} \le \varepsilon_y^q$), respectively. $E_{0,m}$ is the undamaged stiffness of a polymer matrix. The matrix damage is evaluated in each stage and the final matrix damage D_m at each integration, the point is

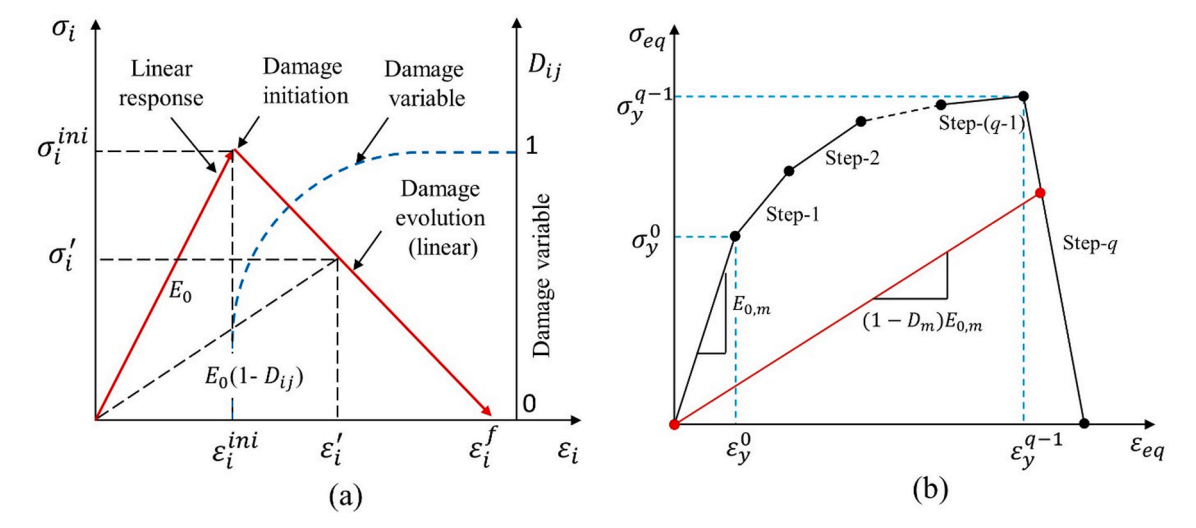


Fig. 5. Damage initiation and evolution laws: (a) impregnated yarns and (b) polymer matrix. Note that σ_i^{ini} , σ_i^i , and E_0 represent stress at failure initiation, instantaneous stress, and undamaged stiffness matrix of impregnated yarn, respectively. $E_{0,m}$, σ_y^0 and ε_y^0 each refers to the undamaged stiffness matrix, yield strength, and corresponding yield strain damage initiation of the matrix.

evaluated based on the maximum matrix damage achieved, given by $D_m = Max(1 - d_m^q)$. The micro-stresses in the polymer matrix region are updated based on the damaged stiffness matrix $C_{ij}^{D,m}$ and micro-strain ε_{ij} , given by Eq. (12).

$$\sigma_{ii}^{m} = (1 - V_v) C_{ii}^{D,m} \varepsilon_{ii} \tag{12}$$

This damage model proposed for matrix failure is more realistic than the ones proposed in our earlier work [14] because it accounts for stochastic variation in matrix failure strength based on the stochastic variation of void content (V_{ν}) .

2.4. Macro-model (FE Model)

To evaluate macro-strains at each integration point due to applied load, FE analysis was conducted at the macro-scale using Abaqus/Explicit software. The macro-strains were used to evaluate the damage state of the FE model in the next time increment. The homogenized macro stresses $\overline{\sigma}$ at each integration, points were determined using a volume averaging method, by adding the individual contributions of all constituents according to their volume proportion in the unit-cell, i.e., Eq. (13).

$$\overline{\sigma} = \sigma^m V_m (1 - V_v) + \sigma^{warp} V_{warp} + \sigma^{fill} V_{fill} + \sigma^{binder} V_{binder}$$
(13)

where σ^m , σ^{warp} , σ^{fill} and σ^{binder} represent micro stresses in the matrix, warp yarn, weft yarn, and binder yarn, respectively. V_m , V_{warp} , V_{fill} and V_{binder} denotes the volume fraction of pure matrix, warp yarn, fill yarn and binder phases, respectively in the unit-cell model. These volume fractions were obtained from CT-scan images of warp, fill and z-binder cross-sections, more details can be found in the reference [14].

3. Experimental evaluations

3.1. Material used

3D orthogonal E-glass woven fabrics (3D-9871, TexTech® Industries, USA) were used in this study. The thickness and areal density of the 3D fabric were 4.3 mm and 5200 GSM. The fabric had 49%, 49%, and 2% fibres along the warp, fill and through-thickness directions, respectively. The fabric had a warp count of 2.8 ends per centimetre (EPCM) and a fill count of 1.9 picks per centimetre (PPCM). The Elium® (188x0, Arkema, France) thermoplastic resin was used to manufacture thermoplastic 3D-FRC using a vacuum-assisted resin infusion process (VARI). More details

on the complete 3D-FRC fabrication process can be found in the references [51-53]. The fibre volume fraction and nominal thickness of cured 3D-FRC were 52% and 4 mm, respectively.

3.2. Testing methods

The notched and unnotched tensile tests were carried out along the warp (0°) and fill (90°) directions, according to ASTM D5766 [54] and D3039 [55] standards, respectively. Note that the ASTM standards recommend an un-notched tensile of 250 \times 25 mm² and a notched tensile test specimen of 200 × 36 mm² with a 6 mm hole diameter, leading to hole diameter (d)-to-width (w) ratio $d_r = 0.166$. Fig. 6(a) shows six testing configurations (i.e., three warp loaded and three fill loaded), divided into the unnotched (Case-A) and notched (Case-B and Case-C) 3D-FRC specimens. In this study, $250 \times 25 \text{ mm}^2$ samples were used for both notched and un-notched configurations. In notched configurations, a 4.1 mm diameter hole was drilled to maintain $d_r = 0.166$ in Case-B, whereas a 10 mm diameter hole was drilled in Case-C with d_r = 0.4, as shown in Fig. 6(b). Table 2 shows the details of six testing configurations, along with dimension, hole size, intact area and d_r . A total of eighteen samples were tested including six for un-notched configuration (Case-A) and twelve for notched configurations (Case-B and Case-C). All tests were carried out at a displacement-controlled load rate of 2 mm/minute using a ZwickRoell hydraulic-driven load frame equipped with a 50 kN load cell (Fig. 6(c)). A minimum of three repeat tests were performed for each configuration investigated in this study. Tensile strains were measured using an axial extensometer (50 mm gauge length) and digital image correlation (DIC). The schematic diagram of boundary conditions is shown in Fig. 6(b).

3.3. Evaluation method

The un-notched and notched performance of resin-infused thermoplastic 3D-FRCs is evaluated using global load (P) versus deflection (δ) curves obtained from load-frame, gross ultimate tensile strength σ_{yy}^{gross} , net axial tensile strength σ_{yy}^{net} , maximum tensile strains obtained from an extensometer. The gross strength was evaluated by dividing the applied load by gross cross-sectional area i.e., $\sigma_{yy}^{gross} = \frac{P}{A_{gross}}$, whereas the net strength was calculated by dividing the applied load by the net cross-sectional area, i.e., $\sigma_{yy}^{net} = \frac{P}{A_{net}} = \frac{P}{i!(w-d)}$. The maximum tensile failure strain was obtained from a 50 mm gauge length extensometer.

In this study, the notch sensitivity was evaluated using d_r and

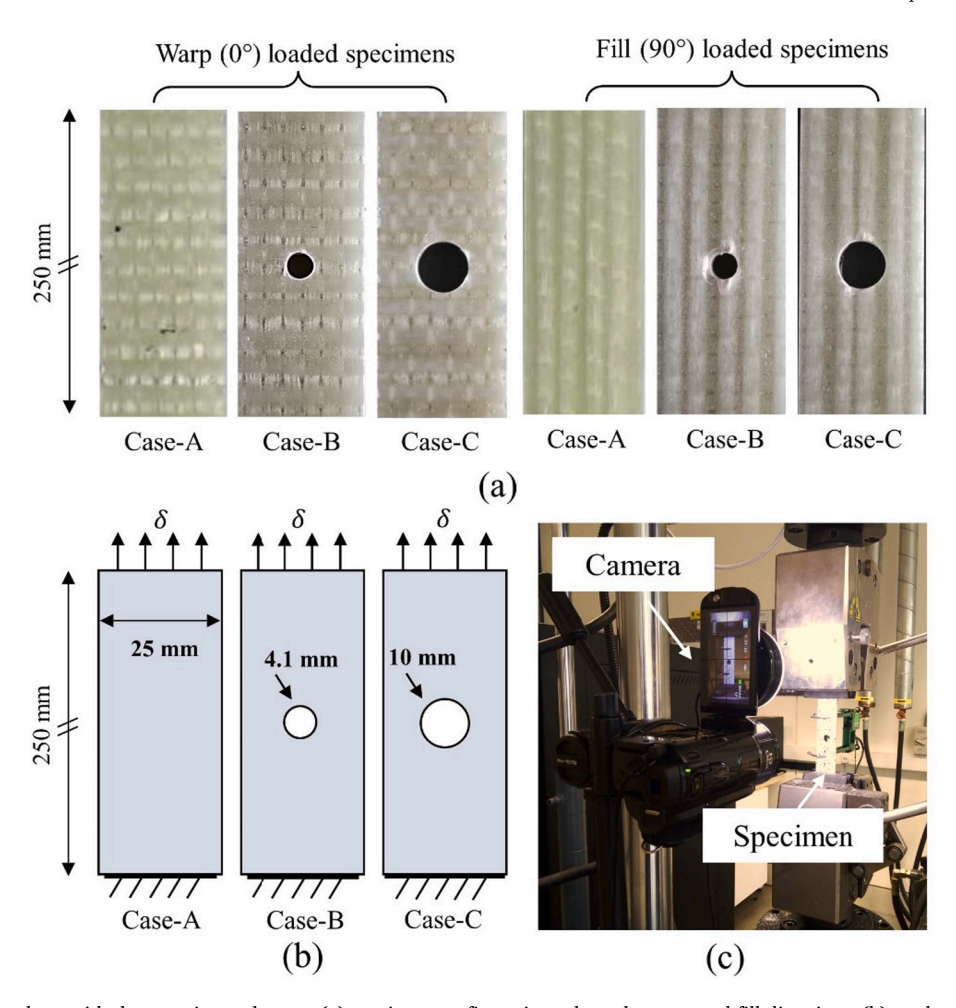


Fig. 6. Tensile specimens along with the experimental setup. (a) specimen configurations along the warp and fill directions, (b) a schematic diagram of specimen dimensions along with boundary conditions applied during testing, and (c) experimental setup.

Table 2 3D-FRC tensile specimen configurations.

Configurations	Details	Hole diameter (mm)	Dimensions $l \times w(mm)$	Intact area A _i (mm ²)	Hole dia. to width ratio d_r
Case-A	3D- Warp 3D-Fill		250×25 250×25	100 100	
Case-B	3D-FIII	4.1	250 × 25	83.6	0.164
Case-D	Warp 3D-Fill	4.1	250 × 25	83.6	0.164
Case-C	3D-	10	250 × 25	60	0.4
	Warp 3D-Fill	10	250 × 25	60	0.4

normalized strength σ_{nn}^{gross} , similar to the work by Muñoz et al. [56]. Here, the normalized strength indicates a ratio between axial gross strength and axial net strength, i.e., $\sigma_{nn}^{gross} = \sigma_{yy}^{gross}/\sigma_{yy}^{net}$. To evaluate the notch sensitivity of 3D-FRC at a specific d_r , notched axial ultimate tensile strength is normalized with un-notched axial ultimate tensile strength measured experimentally. The normalised value was then compared to the ideally *ductile* "notch insensitive" and ideally *brittle* "notch sensitive" curves. The ideal notch insensitive (for a ductile material) and sensitive

(for a brittle material) response is given by Eqs. (14) and (15) [57,58], respectively.

$$\frac{\sigma_{yy}^{gnet}}{\sigma_{yy}^{gross}} = 1 - \left(\frac{d}{w}\right) \tag{14}$$

$$\frac{\sigma_{yy}^{gnet}}{\sigma_{yy}^{gross}} = \left[1 - \left(\frac{d}{w}\right)\right] / K_T \tag{15a}$$

$$K_T = 2 + [1 - (d/w)]^3$$
 (15b)

where d and w refer to hole diameter and specimen width.

4. Numerical simulation

4.1. Numerical implementation of the stochastic progressive damage model

The overall algorithm of the stochastic multiscale progressive damage model is implemented through a VUMAT subroutine. Fig. 7 explains how different length-scale models (described in Section 2) interact with each other for damage prediction within a stochastic, multiscale modelling framework. At the start of the analysis before the application of loads (time = 0), a function within the VUMAT generates uniformly distributed random numbers (for yarn waviness and voids) for each integration point/element (representing unit-cell) in the FE model,

using the Box-Muller transformation algorithm. These random numbers are stored in the state variables (SDVs) and remain constant for each increment to perform stochastic FE analysis. The stochastic micromechanics model evaluates the unique effective elastic constants and strength properties for each unit-cell element in GCS using the stochastic distribution of defects obtained from μ CT. The effective elastic constants are used to evaluate *meso*-stresses in the pure matrix $\overline{\sigma}_{n,m}^{(t)}$ and impregnated yarns $\overline{\sigma}_{n,p}^{(t)}$ for each integration point in GCS. These *meso*-stresses are then transformed with respect to their orientations (yarn orientation and its stochastic distribution) to get *meso*-stresses in LCS. The *meso*-stresses are used to evaluate the damage state of each constituent and update *meso*-stresses at the end of the current time increment. The

S.Z.H. Shah et al.

updated *meso*-stresses are then transformed back into GCS, using Eq. (5). Lastly, the homogenised macro-stresses at each integration point are calculated using the micro-stresses in GCS and the volume fraction of each unit cell constituent. These macro-stresses are fed back into Abaqus to calculate strain increment for the subsequent time increment. The FE simulation has been conducted at a macro-scale using a hexahedral solid element (i.e., C3D8R in Abaqus), with each element representing a full unit cell of 3D orthogonal woven composites. The proposed framework is computationally efficient firstly because the micro-mechanics model for yarn and matrix as well as the *meso*-scale model for the unit-cell is analytical and thus does not require high computational cost associated with FE-based micro and meso- models. Secondly, the global macro

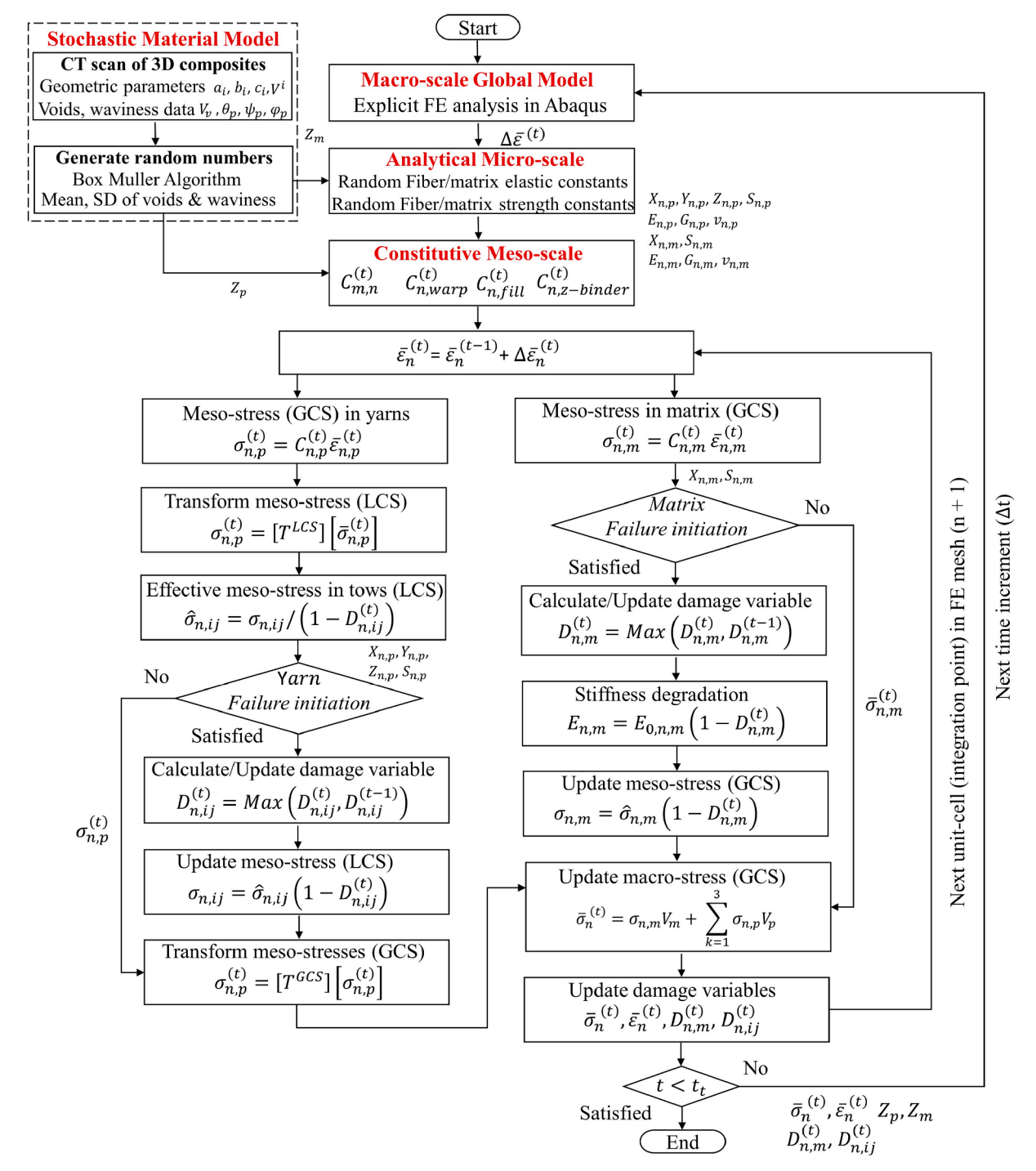


Fig. 7. Overall algorithm for stochastic, multiscale, progressive damage prediction in 3D woven composite.

model uses explicit dynamic FE simulation which is inherently more stable and quicker to converge for damage growth modelling simulations as compared to implicit models. The framework is also easy to implement as part modelling can take place using the existing solid geometry modelling tools available in finite element software like Abaqus or Ansys and does not require third-party tools for explicit modelling of textile geometry and matrix regions. Another thing that should be pointed out is that although we have used X-ray μ CT to obtain the variation in yarn waviness, traditional stereo microscopy of carefully prepared cross-sections may also be used as a suitable alternative if μ CT equipment is not available.

4.2. Finite element model of the notch and un-notch tests

To evaluate the performance of the stochastic, multiscale, progressive damage model, notched and un-notched tensile tests are simulated on 3D-FRCs along the warp (0°) and fill (90°) directions. Fig. 8 shows the geometry, boundary conditions and FE mesh for un-notched (Case-A) and notched (Case-B and Case-C) configurations. The geometry and boundary conditions used in the finite element analysis of the notch and un-notched tensile coupon are shown in Fig. 8(a) and 8(b), respectively. For each configuration, 10 stochastic FE simulations were performed to show variations in ultimate strengths, stress/strain curves and damage responses.

4.3. Material properties

The elastic constants and strength properties of E-Glass fibre and Elium matrix of E-Glass/Elium composites used in the stochastic multiscale progressive damage model are summarized in Table 3.

The critical energy release rates of E-Glass/Elium in longitudinal directions $(G_{1c}^{1+},G_{1c}^{1-})$, in-plane transverse direction $(G_{2c}^{2+},G_{2c}^{2-})$, and out-of-plane transverse direction $(G_{3c}^{3+},G_{3c}^{3-})$, are given in Table 4.

5. Results and discussion

To demonstrate the effectiveness of the proposed stochastic, multiscale, progressive damage model, this section presents three different ${\bf r}$

Table 3 Elastic constants and strength of E-Glass fibre and Elium matrix.

Materials	Material Properties		
E-Glass fibre	Elastic constants [59]	Modulus of Elasticity E_f (GPa)	73
		Modulus of Rigidity G_f (GPa)	30
		Poisson's Ratio v_f	0.22
	Strength properties	Fiber tensile strength (MPa)	2000
	[60]	Fiber compressive strength	1350
		(MPa)	
Elium	Elastic constants	Modulus of Elasticity E_m (GPa) ^c	3.10
matrix		Modulus of Rigidity G_m (GPa)	1.13
		Poisson's Ratio v_m	0.37
	Strength properties	Matrix tensile strength (MPa) c	70
		Matrix compressive strength	130
		(MPa) ^c	
		Matrix shear strength (MPa)	42

^a Reported in literature [59], ^b Reported in literature [61], ^c Reported in literature [60].

Table 4The critical energy release rate of impregnated yarns used in the present study.

	The critical energy release rate	G _{1c} ¹⁺ (N/ mm)	G _{1c} ¹⁻ (N/ mm)	G _{2c} ²⁺ (N/ mm)	G _{2c} ²⁻ (N/ mm)	G _{3c} ³⁺ (N/ mm)	G _{3c} (N/ mm)
-	E-Glass/Elium [62]	60	39.15	1.5	4	1.5	4

types of results. First, the notched and un-notched damage responses of 3D-FRC obtained experimentally are discussed in terms of load/deflection curves, gross strength, net strength, and notched sensitivity. Second, deterministic FE simulation results obtained using the multiscale model proposed in our previous work [14] are compared with experimental data, to highlight the limitations of the existing model. Finally, to overcome the limitations of the existing (deterministic) multiscale model notched and un-notched responses and corresponding damage states predicted by the proposed stochastic FE simulations are compared with experimental data.

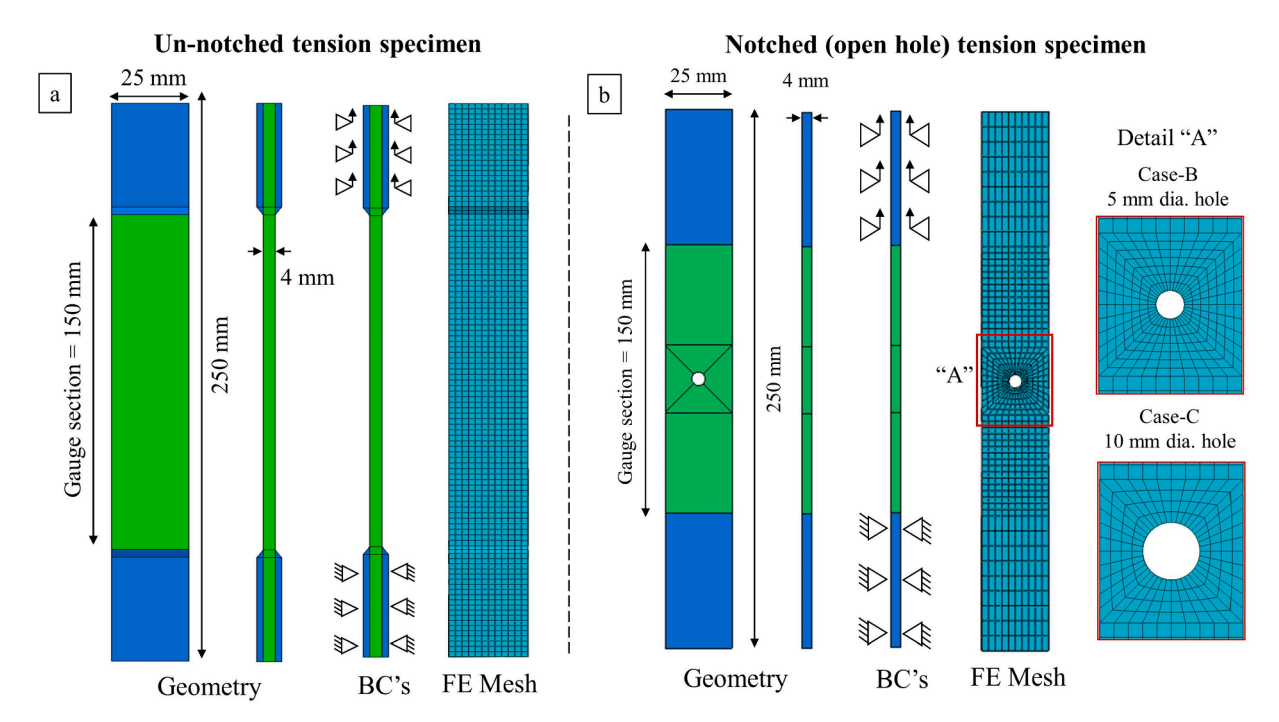


Fig. 8. Schematic of geometry, boundary conditions and FE mesh. (a) un-notched and (b) notched tensile specimens.

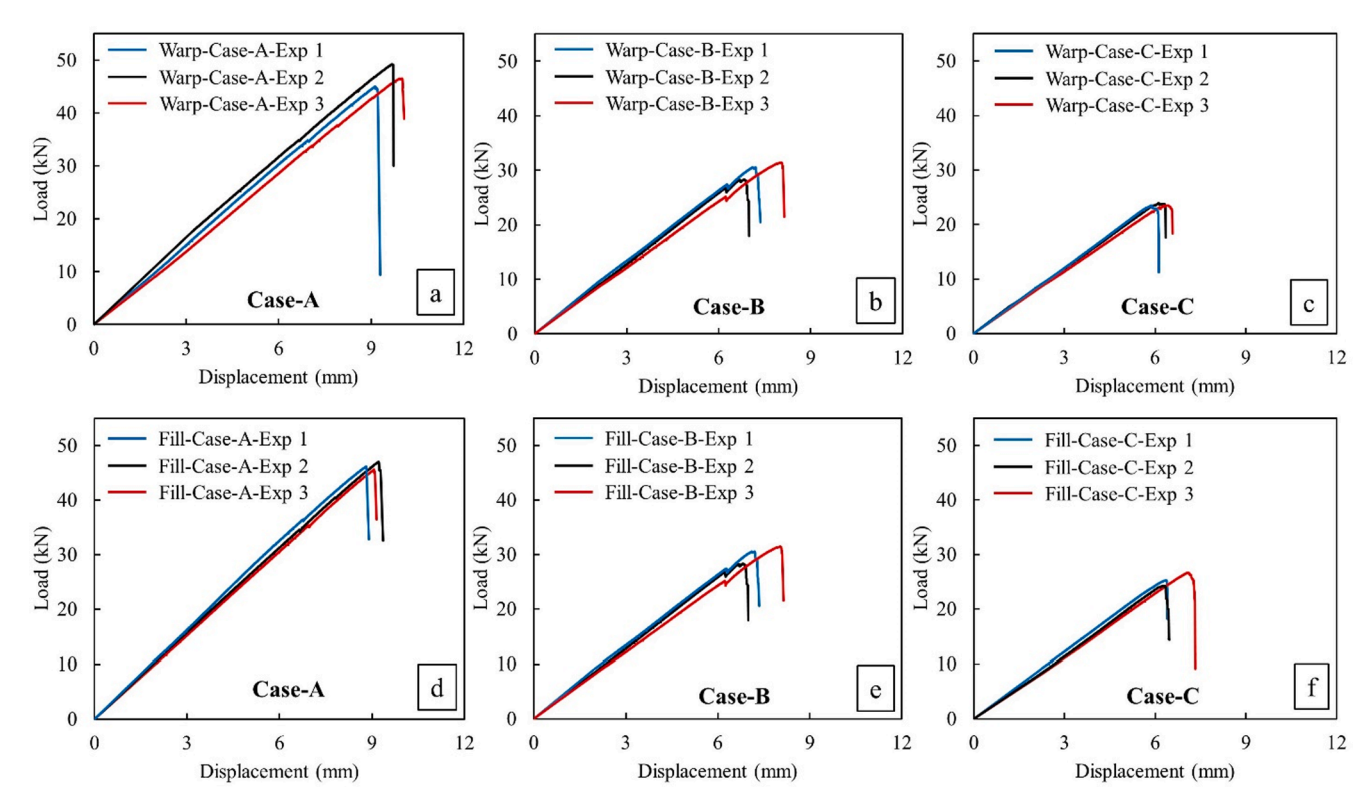


Fig. 9. Load-deflection responses of un-notched and notched 3D-FRC specimens: (a) warp loaded un-notched specimen, (b) warp loaded notched specimen, (c) warp loaded notched specimen, (d) fill loaded un-notched specimen, (e) fill loaded notched specimen, and (f) fill loaded notched specimen.

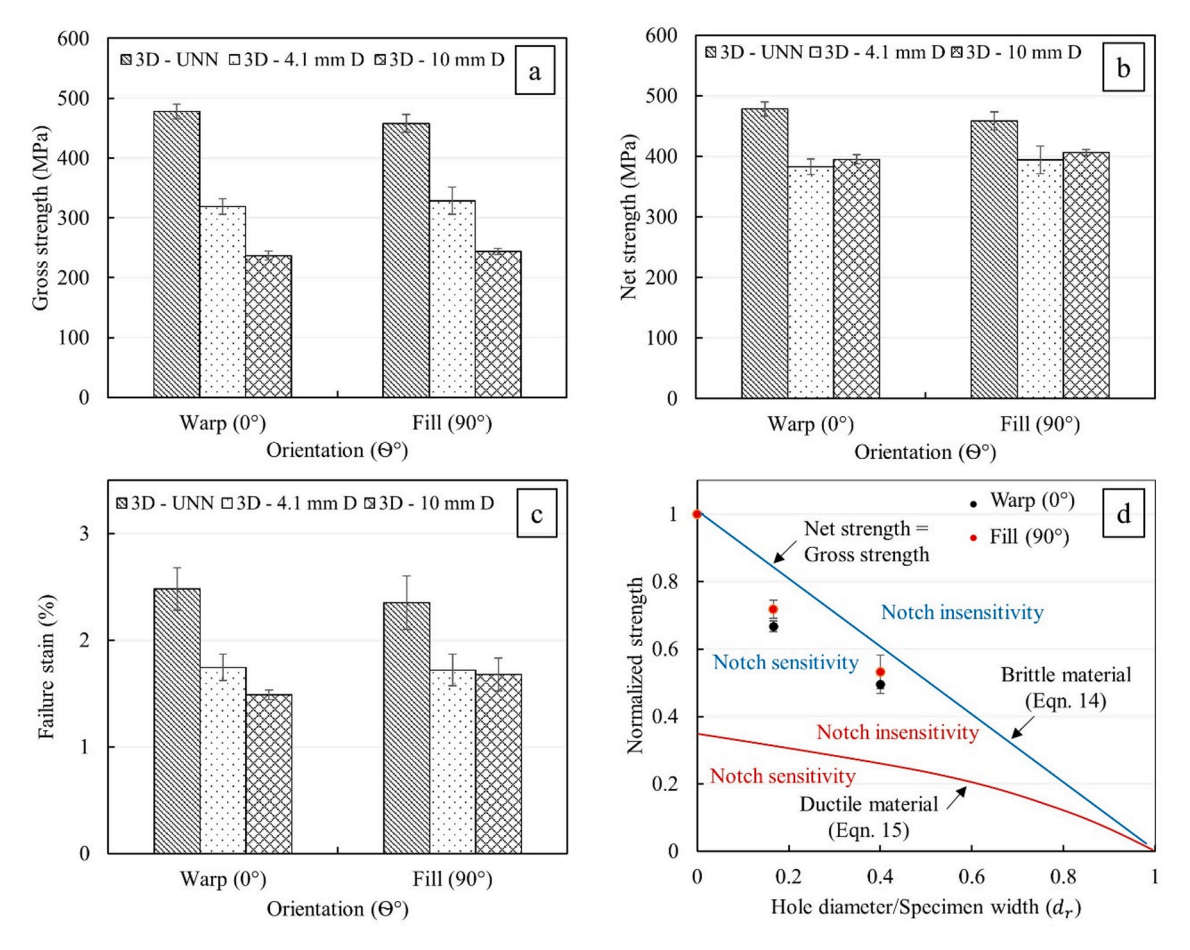


Fig. 10. Comparison of un-notched and notched tensile performance of 3D-FRC: (a) gross strength along the warp and fill direction, (b) net strength along the warp and fill direction, (c) failure strains along the warp and fill direction, and (d) notch sensitivity plot of 3D-FRC with different notch size.

5.1. Experimental un-notched and notched tensile response of 3D-FRC

Fig. 9 shows the un-notched (Case-A) and notched (Case-B and Case-C) load/displacement responses of 3D-FRC along the warp (0°) and fill (90°) directions. A good agreement was achieved in the load/deflection curves obtained from three sets of samples for each (un-notched and notched) configuration. The warp and fill configurations showed nearly identical peak load and load/displacement curves due to similar fibre volume fraction (~49%) in both directions. However, because of the increased waviness induced by the binder yarn, the fill loaded specimens had slightly lower strength. The un-notched configuration showed the highest peak load (48.7 kN). For the notched configurations, the peak load was observed to decrease with an increase in the notch size (e.g., 32.1 kN in Case-B and 24.3 kN in Case-C). All the load/deflection curves showed a nearly linear-elastic response, in the beginning, followed by some nonlinearity at higher loads. The slight reduction in the tensile stiffness of samples can be partially due to 1) the deformation in the ductile Elium matrix and 2) the glass fibre's straightening effects explained by Warren et al. [63].

The notched specimens in Case-B (Fig. 9(b) and (e)), showed the first

Table 5Summary of un-notch and notch tensile performance of 3D-FRC.

Configurations/	Warp spe	ecimens		Fill speci	Fill specimens		
Property	Case-A	Case-B	Case-C	Case-A	Case-B	Case-C	
$F_{max}(kN)$	48.7	31.6	23.7	46.5	32.1	24.3	
$\sigma_{yy}^{gross}(\text{MPa})$	(±3.5) 487	(±4.0) 316	(±3.1) 237	(±2.4) 465	(± 10.0) 321	(±5.1) 243	
$\sigma_{vv}^{net}(\text{MPa})$	(±3.5) 487	(±4.0) 382	(±3.1) 395	(±2.4) 465	(±10.0) 394	(±5.1) 406	
,,	(±3.5)	(±4.0)	(±3.1)	(±2.4)	(±10.0)	(±5.1)	
$\varepsilon_{max}(\%)$	2.48 (±8.8)	1.74 (±7.0)	1.48 (± 3.03)	2.35 (± 4.3)	1.72 (±8.5)	1.68 (±9.1)	

Note: the values in the bracket represent the standard deviation (in percentage) from three specimens for each configuration.

small drop in load at higher displacement (~6 mm in warp and fill specimens), caused by the initiation of transverse matrix cracks. These cracks were subsequently arrested by the ductile matrix and resisted further crack growth along the transverse direction. As a result, the load recovered and reached the second final peak load, followed by the sudden large drop in load upon further propagation of transverse cracks. In comparison, the notched specimens in Case-C (Fig. 9(c) and (f)) exhibited sudden failure due to a small load-bearing area (due to a large notch size), which accrues rapid propagation of transverse cracks. Thus, due to the discontinuous crack propagation and higher load-bearing area, the Case-B samples withstood a high load of 32.1 kN compared to 24.3 kN in Case-C.

Fig. 10 compares gross ultimate tensile strength, tensile failure strain, and notch sensitivity of 3D-FRC considered in this work. The reduction in the gross ultimate tensile strength is almost constant along the warp and fill direction (i.e., up to 35% for Case-B and 51% for Case-C), as shown in Fig. 10(a). This is due to the similar fibre content along both directions, as mentioned earlier. However, in the case of the net ultimate tensile strength (Fig. 10(b)), Case-B and Case-C show up to 21% and 19% reduction. In addition, the presence of a notch affects the failure strain in both directions, each showing up to 27% and 40% reduction in Case-B and Case-C (Fig. 10(c)). Fig. 10(d) shows the notch sensitivity plot for E-Glass/Elium composite, obtained by normalizing the gross strength by the net strength, plotted against d_r . As can be seen in the figure, the normalized strength values are below the blue line representing net strength equal to gross strength. This indicates that the stress concentration (due to the presence of a hole) affects the failure strength of 3D-FRC. Nevertheless, this strength reduction is not significant in a ductile matrix [64], and is partially due to through-thickness reinforcement in 3D fabric architecture. The ultimate tensile load, gross tensile strength, net tensile strength and localized failure strains up to a complete failure in each case along with the standard deviations are summarized in Table 5.

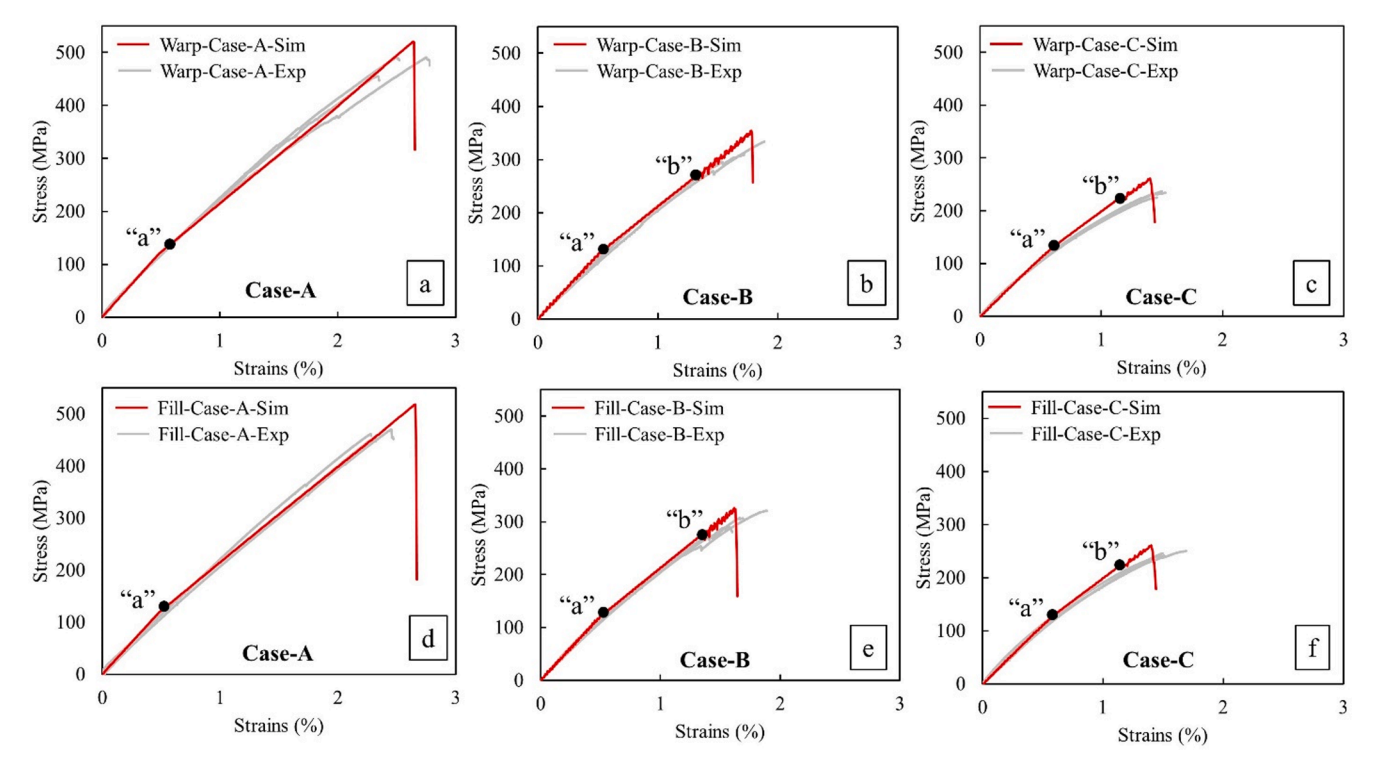


Fig. 11. Experimental and deterministic model prediction for un-notched and notched 3D-FRC tensile specimens: (a) warp loaded un-notched specimen, (b) warp loaded notched specimen, (c) warp loaded notched specimen, (d) fill loaded un-notched specimen, (e) fill loaded notched specimen, and (f) fill loaded notched specimen.

5.2. Comparison of un-notched and notched tensile response (experimental vs. deterministic FE simulation)

Fig. 11 compares un-notched and notched tensile stress/strain curves obtained from experiments and deterministic FE simulations using the multiscale progressive damage model proposed in our earlier publication [14]. The FE simulation was performed along the warp and fill directions. The multiscale model successfully predicted the key characteristics of un-notched and notched tensile stress/strain curves, i.e.,

tensile modulus, and initial linear region followed by nonlinear region. The nonlinear region starts approximately from 0.6 to 0.75% tensile strains (see point "a" in Fig. 11). The transition from linear to nonlinear region corresponds to damage initiation in the matrix. At the onset of matrix damage, the stiffness of the 3D-FRC starts to decrease. Such nonlinear behaviour is also explained by Callus et al. [65], for unnotched specimens. The un-notched specimens undergo a sudden failure after reaching the ultimate tensile strength. In contrast, the notched specimens show progressive failure due to the propagation of the

Table 6
Un-notched and notched ultimate tensile strength from experiments and deterministic multiscale models.

Specimen		Notch size	Warp specimens (Warp specimens (0°)			Fill specimens (90°)		
		d (mm)	Exp.	Sim.	% Diff	Exp.	Sim.	% Diff	
Unnotched	Case-A		487 (±3.5)	507	4.1	465.0 (±2.4)	502	7.9	
Notched	Case-B	4.1	319 (±4.0)	350	9.7	$321.0~(\pm 10.0)$	345	7.5	
	Case-C	10	237 (± 3.1)	262	10.5	243.0 (± 5.1)	258	6.2	

Note: the values in the bracket represent the standard deviation from three specimens for each configuration.

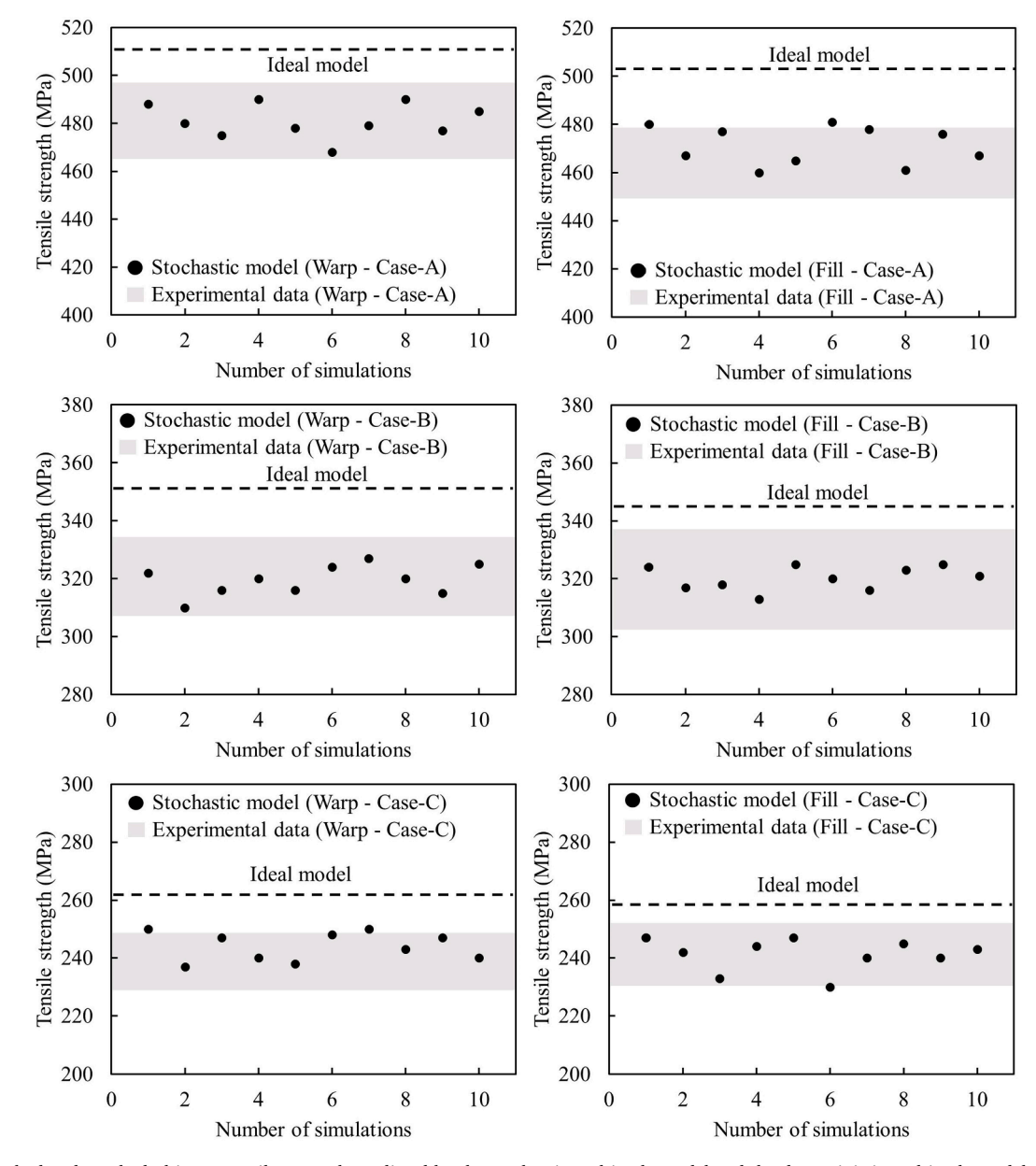


Fig. 12. Un-notched and notched ultimate tensile strength predicted by the stochastic multiscale model and the deterministic multiscale model (ideal model) and their comparison with experimental data: (a) warp specimen, (b) fill specimen, (c) warp specimen, (d) fill specimen, (e) warp specimen, and (d) fill specimen.

transverse matrix cracking in 3D-FRC. In the current study, the transverse matrix crack initiated roughly at 1.3–1.4% tensile strains for case-B, and 1.1–1.2% tensile strain for case-C. The initiation of transverse cracks corresponds to the initiation of fibre failure, highlighted by the slight dip in the stress/strain curve (see point "b" in Fig. 11). These transverse cracks propagate upon further loading, which leads to the complete failure of specimens.

The deterministic, multiscale model over-predicted the un-notched and notched ultimate tensile strength by 5–10 %. This over-prediction is primarily due to the *idealised* unit-cell model, i.e., the impregnated yarns perpendicular to each other, no waviness in impregnated yarns, and no voids in resin rich-pockets. All these factors significantly affect the elastic constants and strength properties of FRC, which accrue inaccuracies in the predicted ultimate tensile strength. Table 6 summarizes the comparison of experimental and FE simulation results, along with the relative percentage difference in the predicted notch and unnotched ultimate tensile strength.

5.3. Improvements in predictive accuracy through stochastic model

Fig. 12 compares the un-notched and notched ultimate tensile strength predicted by the proposed stochastic multiscale model with both the experimental data and the deterministic multiscale simulation. A total of 10 stochastic FE simulations were performed for each specimen configuration and predicted notched and un-notched ultimate strength is included in the figure. The deterministic multiscale model, named as an ideal model in the figure, over-predicted the ultimate tensile strength in all cases. Meanwhile, the stochastic model successfully predicted the notched and un-notched ultimate tensile strength (represented by black dots), which is within the experimental bounds (represented by a grey colour region). Table 7 summarizes the ultimate tensile strength obtained from the experiment and FE simulations, along with their coefficient of variance (COV) and percentage difference. The maximum COV in the ultimate tensile strength predicted from the stochastic model is 1.7, 1.6, and 2.3 % for Case-A, Case-B and Case-C, respectively. This is within the experimental bounds. The maximum relative percentage of difference in the predicted tensile strength is <3%. These results elucidate that the proposed stochastic multiscale

Table 7Un-notched and notched ultimate tensile strength from experiments and stochastic models.

Specimen		Notch size d, (mm)	Warp specimens	Warp specimens (0°))		
			Exp.	Sim.	% Diff	Exp.	Sim.	% Diff	
Unnotched	Case-A		487 (±3.5)	481.0 (±1.4)	1.2	465.0 (±2.4)	471.0 (±1.7)	1.3	
Notched	Case-B	Dia 4.1	$319 (\pm 4.0)$	$320.5 (\pm 1.6)$	0.5	$321.0~(\pm 10.0)$	$323.3 (\pm 1.5)$	0.7	
	Case-C	Dia 10	237 (± 3.1)	244.0 (± 2.0)	2.9	243.0 (± 5.1)	241.0 (\pm 2.3)	0.9	

Note: the values in the bracket represent the standard deviation from three specimens for each configuration.

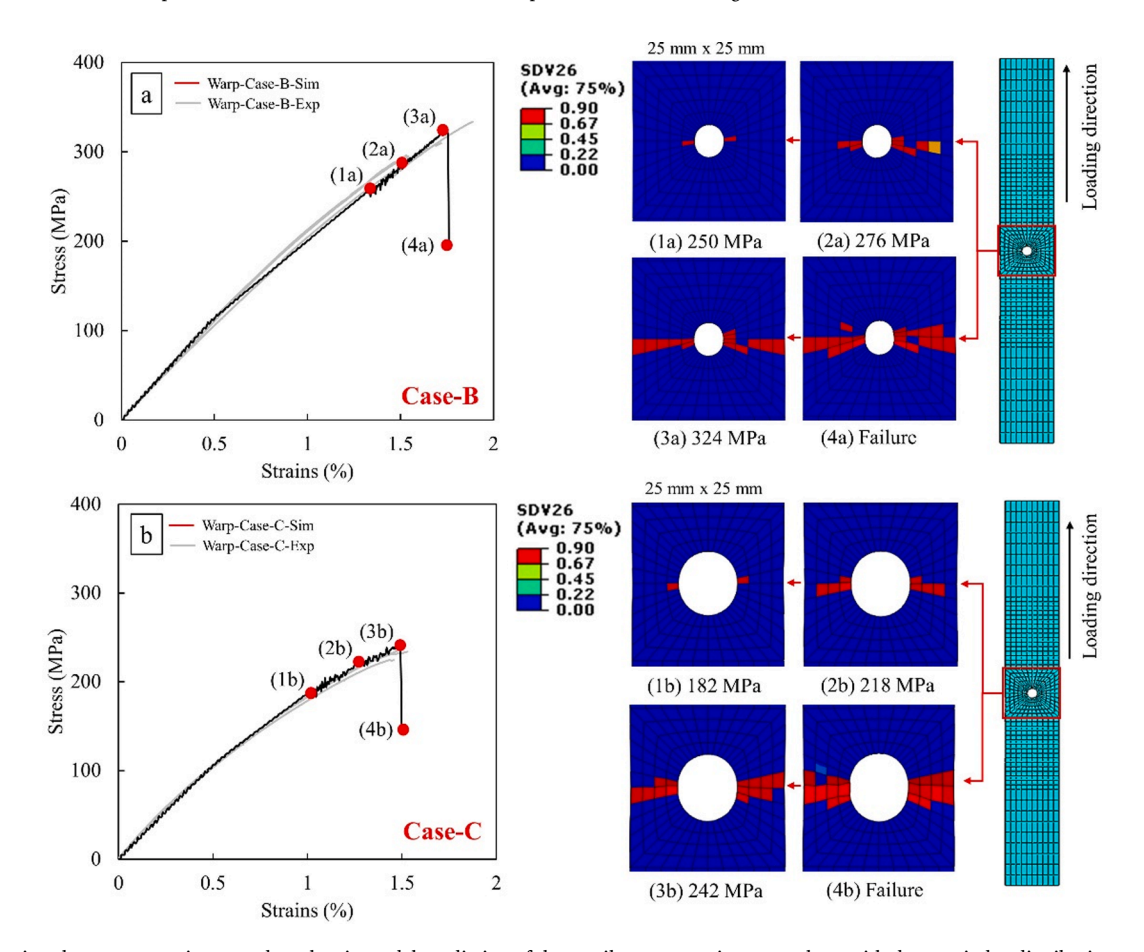


Fig. 13. Comparison between experiment and stochastic model prediction of the tensile stress-strain curve, along with damage index distribution at different stress levels: (a) warp-loaded notched specimen (Case-B) and (b) warp-loaded notched specimen (Case-C).

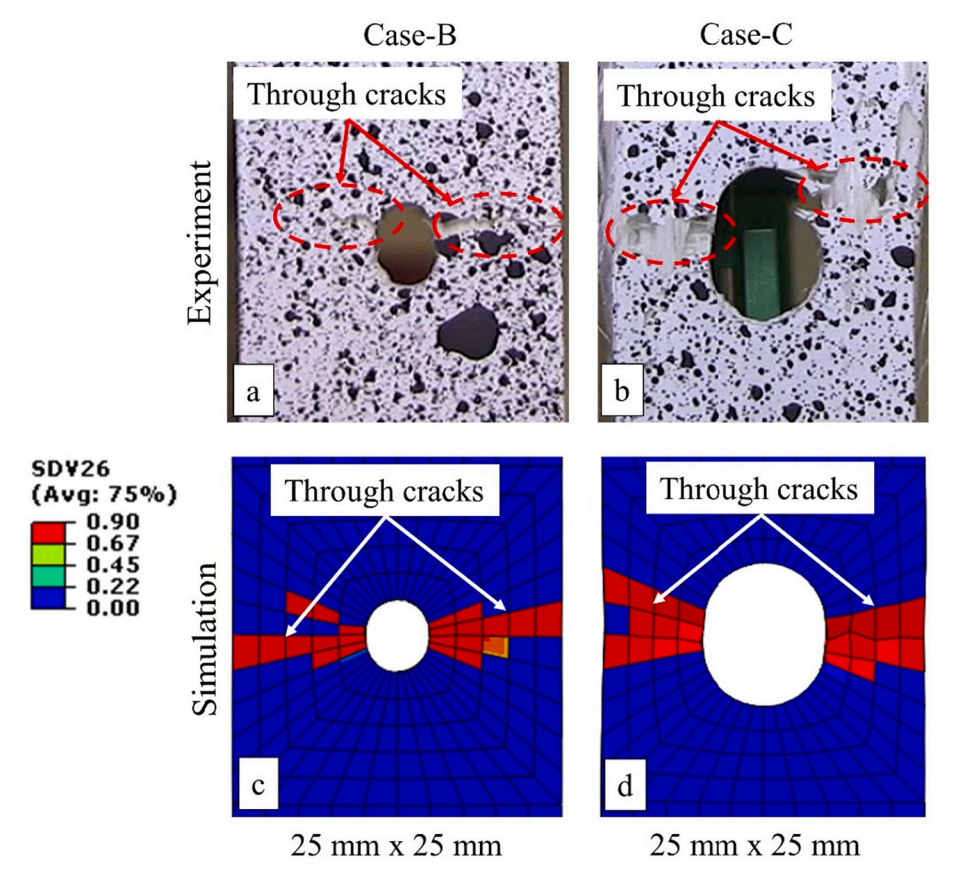


Fig. 14. Comparison between digital image correlation (DIC) measurement and stochastic FE simulation at failure: (a) DIC (Case-B), (b) DIC (Case-C), (c) simulation (Case-B), and (d) simulation (Case-C).

model significantly improved the prediction accuracy over the deterministic multiscale model based on *ideal* unit-cell.

5.4. Comparison of damage evolution states (experimental vs. Stochastic FE simulation)

The stress/strain curves and corresponding damage index (state) distributions obtained from stochastic FE simulation of notched specimens (Case-B and Case-C) at different stress levels are shown in Fig. 13. In the figure, the damage index distributions (points a-d) are taken from a $25 \times 25 \text{ mm}^2$ section of a typical simulated notched specimen and the damage variable (SDV26) indicates the extent of combined longitudinal/transverse fibre failure. Note that the stochastic model prediction varies from specimen to specimen, consistent with a specimen-tospecimen variation in actual testing. The stress/strain curve depicts a linear response until 0.75 % strains, followed by the nonlinear region due to damage growth. The first damage state distributions (at points 1a and 1b) show the initiation of a transverse crack, at the highly stressconcentration area (i.e., at a circular notch) in the form of longitudinal fibre failure due to tensile load. The second damage state distribution (at points 2a and 2b) shows the proportion of transverse cracks (fibre damage) until it reaches the peak stress value, i.e., 324 MPa (Case-B) and 242 MPa (Case-C). In the third damage state distribution (at points 3a and 3b), the transverse cracks reach the maximum crack length, which immediately results in the sudden failure of the 3D-FRC (at points 4a and 4b).

The final damage state of notched specimens obtained from experiments and stochastic FE simulation is compared in Fig. 14. The notched specimens failed due to the propagation of transverse cracks initiated due to intensive fibre failure in a near-circular notch. The 3D-FRC failed in the form of through cracks upon extensive fibre failure. The stochastic

multiscale model successfully captured the final damage states observed experimentally.

Fig. 15 compares the damage index distributions (at failure) obtained from the deterministic multiscale model (reference) and five consecutive runs of the proposed stochastic multiscale models. Each image is taken from a 25 \times 25 mm² section of the simulated specimen. The final failure in un-notched and notched specimens occurs when fibre failure has progressed across the width of the specimen. Although the deterministic model predicted the ideally desired damage patterns in both the un-notched and notched specimens, i.e., matrix and fibre failure in the guage section, along the width of the specimens as well as symmetric nature of damage owing to the same elastic constants and strength properties of all elements. The reference model was unable to fully capture a specimen-to-specimen variation, meaning that the simulated specimens from several simulations fail exactly at the same location and with the same pattern. In contrast, the damage index distribution at failure predicted by the stochastic model was somewhat unsymmetric, thus being more consistent with experimental observation. The discrete damage patterns in Fig. 15 are associated with the stochastic distribution of varn waviness and voids, which are expected to appear during the manufacturing process. The presence of these inhomogeneities locally improves or degrades the elastic constants and strength properties of 3D-FRC. As a result, the initial transverse crack (upon fibre failure) and subsequent propagation depend on a local variation in the inhomogeneities. Such discrete damage patterns are consistent with experimental observations in all configurations tested in this study. Again, these results elucidate that the stochastic, multiscale, progressive damage model significantly improves the prediction accuracy over the deterministic multiscale model.

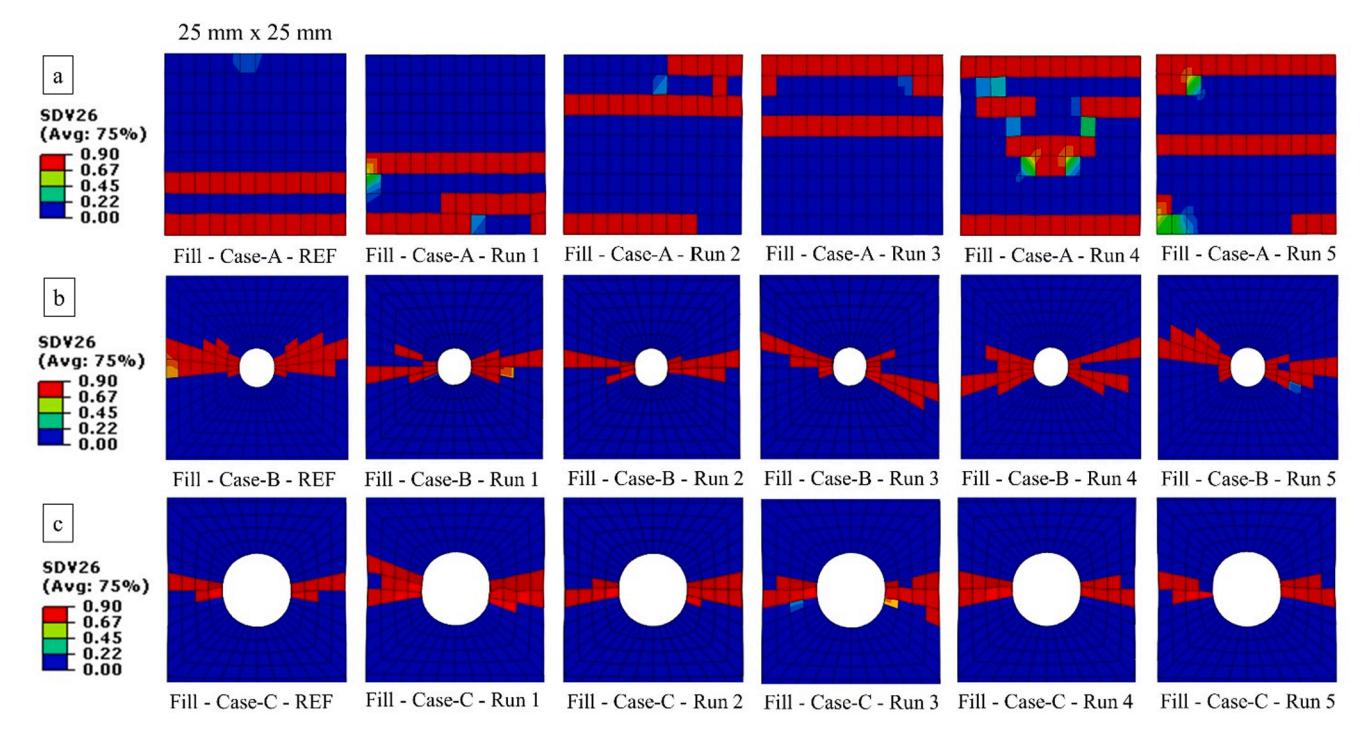


Fig. 15. Damage index distribution around the notch at failure, obtained from the reference (deterministic multiscale) model and five consecutive runs of the stochastic multiscale model: (a) fill-loaded un-notched specimen (Case-A), (b) fill-loaded notched specimen (Case-B), and (c) fill-loaded notched specimen (Case-C).

6. Conclusion

A novel stochastic, multiscale, progressive damage model is proposed to predict the damage response of a three-dimensional (3D) orthogonal woven composite. The spatial distribution of manufacturing-induced defects (waviness in impregnated varn and voids) was obtained from a limited set of micro-computed tomography (µCT) images. This information was used to calculate the stochastic distribution of material properties at the micro- and meso-levels, which consequently results in a local variation of the stress and strain within the macro-model. The model predictions were validated with experimental results and were also compared with our earlier deterministic multiscale model. Excellent correlation was achieved between experiments and stochastic FE simulations. The predicted ultimate tensile strength from the stochastic model was within 3% of the actual average ultimate strength from physical experiments. Our proposed stochastic, multiscale, progressive damage model provides a more accurate estimate of tensile response and corresponding damage evolution in both un-notched and notched 3D woven composites.

The experiments and stochastic FE simulations revealed that unnotched specimens failed abruptly after reaching the peak load. In contrast, notched specimens failed progressively due to the propagation of transverse cracks, i.e., failure starts with the initiation of transverse cracks upon fibre failure (at the notch tip) and subsequent crack propagation of the crack across the width of the specimen. The FE simulation results elucidate that the proposed stochastic multiscale progressive damage model, developed based on a combination of stochastic manufacturing defects, multiscale model, and continuum damage mechanics, can effectively predict the ultimate tensile strength, crack propagation, and final failure of notched 3D woven composites. The developed model will be beneficial in designing robust composite structures and achieving better usage of textile composites as it is accurate as well as computationally efficient. The proposed framework is expected to solve large parts of 50,000 elements in around 3 h.

 $CRediT\ authorship\ contribution\ statement$

S.Z.H. Shah: Conceptualization, Methodology, Formal analysis,

Investigation, Visualization, Writing – original draft, Funding acquisition. Juhyeong Lee: Writing – review & editing. P.S.M. Megat-Yusoff: Supervision, Investigation, Project administration. Syed Zahid Hussain: Resources. T. Sharif: Investigation, Writing – review & editing. R. S Choudhry: Supervision, Methodology, Investigation, Writing – original draft, Writing – review & editing.

Declaration of Competing Interest

The authors declare that they have no known competing financial interests or personal relationships that could have appeared to influence the work reported in this paper.

Data availability

Data will be made available on request.

Acknowledgements

The authors would like to acknowledge the financial support provided by Universiti Teknologi PETRONAS (grant number 015LA0-031). The authors would also like to acknowledge the support of Dr. Pierre Gerard from Arkema and Dr. Sharp Keith in acquiring Elium® resin and 3D fabric for this research work.

References

- Kaddour A, Hinton M. Progress in failure criteria for polymer matrix composites: A view from the first World-Wide Failure Exercise (WWFE). Failure Mechanisms in Polymer Matrix Composites. Elsevier; 2010. p. 3–25.
- [2] Kaddour A, Hinton M, Smith P, Li S. The background to the third world-wide failure exercise. J Compos Mater 2013;47:2417–26.
- [3] Vignoli LL, Savi MA, Pacheco PM, Kalamkarov AL. Multiscale approach to predict strength of notched composite plates. Compos Struct 2020;253:112827.
- [4] Ud Din I, Tu S, Hao P, Panier S, Khan KA, Umer R, et al. Sequential damage study induced in fiber reinforced composites by shear and tensile stress using a newly developed Arcan fixture. J Mater Res Technol 2020;9:13352–64.
- [5] Green S, Matveev M, Long A, Ivanov D, Hallett S. Mechanical modelling of 3D woven composites considering realistic unit cell geometry. Compos Struct 2014; 118:284–93.

- [6] Ansar M, Xinwei W, Chouwei Z. Modeling strategies of 3D woven composites: a review. Compos Struct 2011;93:1947–63.
- [7] Shah SZH, Choudhry RS, Khan LA. Challenges in compression testing of 3D angle-interlocked woven-glass fabric-reinforced polymeric composites. ASTM J Test Eval 2017;5:1502-23
- [8] Shah SZH, Megat Yusoff PSM, Karuppanan S, Sajid Z. Elastic constants prediction of 3D fiber-reinforced composites using multiscale homogenization. Processes 2020:8
- [9] Feyel F. A multilevel finite element method (FE2) to describe the response of highly non-linear structures using generalized continua. Comput Methods Appl Mech Eng 2003;192:3233–44.
- [10] Wang B, Fang G, Wang H, Liang J, Dai F, Meng S. Uncertainty modelling and multiscale simulation of woven composite twisted structure. Compos Sci Technol 2022:217
- [11] Bostanabad R, Liang B, Gao J, Liu WK, Cao J, Zeng D, et al. Uncertainty quantification in multiscale simulation of woven fiber composites. Comput Methods Appl Mech Eng 2018;338:506–32.
- [12] Spahn J, Andrä H, Kabel M, Müller R. A multiscale approach for modeling progressive damage of composite materials using fast Fourier transforms. Comput Methods Appl Mech Eng 2014;268:871–83.
- [13] Huang W, Xu R, Yang J, Huang Q, Hu H. Data-driven multiscale simulation of FRP based on material twins. Compos Struct 2021;256.
- [14] Shah SZH, Megat-Yusoff P, Karuppanan S, Choudhry R, Sajid Z. Multiscale damage modelling of 3D woven composites under static and impact loads. Compos Part A: Appl Sci Manuf 2021;151:106659.
- [15] Turner P, Liu T, Zeng X, Brown K. Three-dimensional woven carbon fibre polymer composite beams and plates under ballistic impact. Compos Struct 2018;185: 483-05
- [16] Tao W, Zhu P, Xu C, Liu Z. Uncertainty quantification of mechanical properties for three-dimensional orthogonal woven composites. Part II: Multiscale simulation. Compos Struct, 235; 2020.
- [17] Han J, Wang R, Hu D, Bao J, Liu X, Guo X. A novel integrated model for 3D braided composites considering stochastic characteristics. Compos Struct 2022;286.
- [18] Ge L, Li H, Zhang Y, Zhong J, Chen Y, Fang D. Multiscale viscoelastic behavior of 3D braided composites with pore defects. Compos Sci Technol 2022;217.
- [19] Bhattacharyya R, Adams D. Multiscale analysis of multi-directional composite laminates to predict stiffness and strength in the presence of micro-defects. Compos Part C: Open Access 2021:6.
- [20] Pankow M, Justusson B, Riosbaas M, Waas AM, Yen CF. Effect of fiber architecture on tensile fracture of 3D woven textile composites. Compos Struct 2019;225.
- [21] Zhou X-Y, Qian S-Y, Wang N-W, Xiong W, Wu W-Q. A review on stochastic multiscale analysis for FRP composite structures. Compos Struct 2022;284.
- [22] Bhattacharyya R, Mahadevan S, Basu PK. Computationally efficient multiscale modeling for probabilistic analysis of CFRP composites with micro-scale spatial randomness. Compos Struct 2022;280.
- [23] Shah SZH, Karuppanan S, Megat-Yusoff P, Sajid Z. Impact resistance and damage tolerance of fiber reinforced composites: a review. Compos Struct 2019;217: 100-21
- [24] Gao Z, Chen L. A review of multi-scale numerical modeling of three-dimensional woven fabric. Compos Struct 2021;263:113685.
- [25] Zhang D, Waas AM, Yen C-F. Progressive damage and failure response of hybrid 3D textile composites subjected to flexural loading, part II: Mechanics based multiscale computational modeling of progressive damage and failure. Int J Solids Struct 2015;75–76:321–35.
- [26] Shi D, Teng X, Jing X, Lyu S, Yang X. A multi-scale stochastic model for damage analysis and performance dispersion study of a 2.5D fiber-reinforced ceramic matrix composites. Compos Struct 2020:248.
- [27] Zhou L, Chen M, Liu C, Wu H. A multi-scale stochastic fracture model for characterizing the tensile behavior of 2D woven composites. Compos Struct 2018; 204:536–47.
- [28] Wang H, Wang Z-w. Quantification of effects of stochastic feature parameters of yarn on elastic properties of plain-weave composite – Part 2: Statistical predictions vs. mechanical experiments. Compos A Appl Sci Manuf 2016;84:147–57.
- [29] Wang P, Lei H, Zhu X, Chen H, Wang C, Fang D. Effect of manufacturing defect on mechanical performance of plain weave carbon/epoxy composite based on 3D geometrical reconstruction. Compos Struct 2018;199:38–52.
- [30] Vanaerschot A, Cox BN, Lomov SV, Vandepitte D. Experimentally validated stochastic geometry description for textile composite reinforcements. Compos Sci Technol 2016;122:122–9.
- [31] Balokas G, Kriegesmann B, Czichon S, Rolfes R. Stochastic modeling techniques for textile yarn distortion and waviness with 1D random fields. Compos Part A: Appl Sci Manuf 2019;127.
- [32] Patel DK, Waas AM, Yen C-F. Direct numerical simulation of 3D woven textile composites subjected to tensile loading: an experimentally validated multiscale approach. Compos B Eng 2018;152:102–15.
- [33] Patel DK, Waas AM, Yen C-F. Compressive response of hybrid 3D woven textile composites (H3DWTCs): an experimentally validated computational model. J Mech Phys Solids 2019;122:381–405.
- [34] Song S, Waas AM, Shahwan KW, Xiao X, Faruque O. Braided textile composites under compressive loads: Modeling the response, strength and degradation. Compos Sci Technol 2007;67:3059–70.
- [35] Huang T, Gong Y. A multiscale analysis for predicting the elastic properties of 3D woven composites containing void defects. Compos Struct 2018;185:401–10.
- [36] Huang T, Gao J, Sun Q, Zeng D, Su X, Kam Liu W, et al. Stochastic nonlinear analysis of unidirectional fiber composites using image-based microstructural uncertainty quantification. Compos Struct 2021;260.

- [37] Peng X, Ye T, Li J, Wu H, Jiang S, Chen G. Multi-scale uncertainty quantification of composite laminated plate considering random and interval variables with data driven PCE method. Mech Adv Mater Struct 2020;1–11.
- [38] Balokas G, Czichon S, Rolfes R. Neural network assisted multiscale analysis for the elastic properties prediction of 3D braided composites under uncertainty. Compos Struct 2018;183:550–62.
- [39] Pitchai P, Jha NK, Nair RG, Guruprasad PJ. A coupled framework of variational asymptotic method based homogenization technique and Monte Carlo approach for the uncertainty and sensitivity analysis of unidirectional composites. Compos Struct 2021;263.
- [40] Balasubramani NK, Zhang B, Chowdhury NT, Mukkavilli A, Suter M, Pearce GM. Micro-mechanical analysis on random RVE size and shape in multiscale finite element modelling of unidirectional FRP composites. Compos Struct 2022;282.
- [41] Zhi J, Tay T-E. Computational structural analysis of composites with spectral-based stochastic multi-scale method. Multiscale Multidiscipl Model Exp Des 2018;1: 103-18
- [42] Huang W, Causse P, Brailovski V, Hu H, Trochu F. Reconstruction of mesostructural material twin models of engineering textiles based on Micro-CT Aided Geometric Modeling. Compos Part A: Appl Sci Manuf 2019;124.
- [43] Wintiba B, Vasiukov D, Panier S, Lomov SV, Ehab Moustafa Kamel K, Massart TJ. Automated reconstruction and conformal discretization of 3D woven composite CT scans with local fiber volume fraction control. Compos Struct 2020;248.
- [44] Zeng Q, Sun L, Ge J, Wu W, Liang J, Fang D. Damage characterization and numerical simulation of shear experiment of plain woven glass-fiber reinforced composites based on 3D geometric reconstruction. Compos Struct 2020;233.
- [45] ASTM D3171-99, Standard Test Methods for Constituent Content of Composite Materials, ASTM International, West Conshohocken, PA, 1999; 1999. www.astm.org.
- [46] Box G. ME muller in annals of math. Stat 1958;29:610-1.
- [47] Shah S, Lee J. Stochastic lightning damage prediction of carbon/epoxy composites with material uncertainties. Compos Struct 2022;282:115014.
- [48] El-Hajjar RF, Petersen DR. Gaussian function characterization of unnotched tension behavior in a carbon/epoxy composite containing localized fiber waviness. Compos Struct 2011;93:2400–8.
- [49] Chamis CC. Simplified composite micromechanics equations for hygral, thermal and mechanical properties. SAMPE O 1984:4:14–33.
- [50] Xu L, Jin CZ, Ha SK. Ultimate strength prediction of braided textile composites using a multi-scale approach. J Compos Mater 2014;49:477–94.
- [51] Shah SZH, Megat-Yusoff P, Karuppanan S, Choudhry R, Ahmad F, Sajid Z, et al. Performance comparison of resin-infused thermoplastic and thermoset 3D fabric composites under impact loading. Int J Mech Sci 2020;189:105984.
- [52] Shah SZH, Megat-Yusoff PSM, Karuppanan S, Choudhry RS, Ahmad F, Sajid Z. Mechanical properties and failure mechanisms of novel resin-infused thermoplastic and conventional thermoset 3D fabric composites. Appl Compos Mater 2021; 515–45.
- [53] Shah SZH, Megat-Yusoff PSM, Choudhry RS, Sajid Z, Din IU. Experimental investigation on the quasi-static crush performance of resin-infused thermoplastic 3D fibre-reinforced composites. Compos Commun 2021;28:100916.
- [54] ASTM D5766 / D5766M-11(2018), Standard Test Method for Open-Hole Tensile Strength of Polymer Matrix Composite Laminates, ASTM International, West Conshohocken, PA; 2018. www.astm.org.
- [55] Astm. D3039/D3039M-17 standard test method for tensile properties of polymer. Matrix Compos Mater 2017.
- [56] Muñoz R, Martínez V, Sket F, González C, Llorca J. Mechanical behavior and failure micromechanisms of hybrid 3D woven composites in tension. Compos A Appl Sci Manuf 2014;59:93–104.
- [57] Saleh MN, Wang Y, Yudhanto A, Joesbury A, Potluri P, Lubineau G, et al. Investigating the potential of using off-axis 3D woven composites in composite joints' applications. Appl Compos Mater 2016;24:377–96.
- [58] Shah SZH, Megat-Yusoff PSM, Sharif T, Hussain SZ, Choudhry RS. Off-axis tensile performance of notched resin-infused thermoplastic 3D fibre-reinforced composites. Mech Mater 2022;175.
- [59] Kinvi-Dossou G, Matadi Boumbimba R, Bonfoh N, Koutsawa Y, Eccli D, Gerard P. A numerical homogenization of E-glass/acrylic woven composite laminates: application to low velocity impact. Compos Struct 2018;200:540–54.
- [60] Liu Y, Straumit I, Vasiukov D, Lomov SV, Panier S. Prediction of linear and nonlinear behavior of 3D woven composite using mesoscopic voxel models reconstructed from X-ray micro-tomography. Compos Struct 2017;179:568–79.
- [61] Kazemi ME, Shanmugam L, Lu D, Wang X, Wang B, Yang J. Mechanical properties and failure modes of hybrid fiber reinforced polymer composites with a novel liquid thermoplastic resin, Elium®. Compos A Appl Sci Manuf 2019;125:105523.
- [62] Zhang D, Waas AM, Yen C-F. Progressive damage and failure response of hybrid 3D textile composites subjected to flexural loading, part II: mechanics based multiscale computational modeling of progressive damage and failure. Int J Solids Struct 2015;75:321–35.
- [63] Warren KC, Lopez-Anido RA, Vel SS, Bayraktar HH. Progressive failure analysis of three-dimensional woven carbon composites in single-bolt, double-shear bearing. Compos B Eng 2016;84:266–76.
- [64] Shah SZH, Megat-Yusoff P, Karuppanan S, Choudhry R, Ud Din I, Othman A, et al. Compression and buckling after impact response of resin-infused thermoplastic and thermoset 3D woven composites. Compos B Eng 2021;207:108592.
- [65] Callus P, Mouritz A, Bannister MK, Leong K. Tensile properties and failure mechanisms of 3D woven GRP composites. Compos A Appl Sci Manuf 1999;30: 1277–87.